

GRANT - LEWIS P-81

IN-6269

d/s V1610109  
= jms

**COLLEGE  
OF  
ENGINEERING**

Semi-Annual Status Report  
on  
NASA Grant No. NAG 3-593

Thermodynamic Evaluation of Transonic Compressor Rotors  
Using the Finite Volume Approach

for the period  
12/20/85 - 5/31/86

by  
Stephen Nicholson  
Instructor  
and  
John Moore  
Professor of Mechanical Engineering  
Principal Investigator



**VIRGINIA  
POLYTECHNIC  
INSTITUTE  
AND  
STATE  
UNIVERSITY**

(NASA-CR-176840) THERMODYNAMIC EVALUATION  
OF TRANSONIC COMPRESSOR ROTORS USING THE  
FINITE VOLUME APPROACH Semiannual Status  
Report, 20 Dec. 1985 - 31 May 1986 (Virginia  
Polytechnic Inst. and State Univ.) 81 p

N86-26546

Unclas  
G3/34 43118

BLACKSBURG,  
VIRGINIA

Semi-Annual Status Report  
on  
NASA Grant No. NAG 3-593

Thermodynamic Evaluation of Transonic Compressor Rotors  
Using the Finite Volume Approach

for the period  
12/20/85 - 5/31/86

by  
Stephen Nicholson  
Instructor  
and  
John Moore  
Professor of Mechanical Engineering  
Principal Investigator

Grantee Institution -  
NASA Lewis Research Center  
21000 Brookpark Road  
Cleveland, Ohio 44135

Turbomachinery Research Group  
Report No. JM/86-2

Mechanical Engineering Department  
Virginia Polytechnic Institute and State University  
Blacksburg, Virginia 24061

V1610109

## ABSTRACT

This report documents progress made in refining and improving <sup>the</sup> finite-volume explicit time marching method (1, 2, and 3) during the time period from January to May 1986. The work is done under NASA grant NAG 3-593. Previously, extension had been made to the finite volume method to

1. improve the accuracy of the calculation of total pressure in inviscid flow (1).
2. extend the method to allow the calculation of laminar and turbulent boundary layers in internal flows (2). <sup>AND</sup>
3. improve the shock capturing properties of the method by introducing a Mach number dependent interpolation scheme for the pressure used in the calculating the density (3).

The current work extends these developments by

1. using the new pressure interpolation scheme in two dimensional viscous calculations,
2. including a more complete description of the viscous stresses,
3. introducing a criteria for the transverse upwind differencing which is a function of the ratio of transverse and streamwise mass fluxes, <sup>AND</sup>
4. allowing the calculation of internal flow where boundary layers are present on both wall of the duct.

Specifically, this report is broken up into three sections. Section-1-discusses-in-detail the manner in which the viscous stresses are evaluated in the non-orthogonal, non-uniform grid. <sup>IS DETAILED</sup> Section-2-in-<sup>IS INJECTION</sup> investigates the convergence and presents results for calculations of laminar flow in a converging duct. <sup>AND PRESENT</sup>

Section 3 presents results for calculations of transonic turbulent flow in a converging-diverging  
<sup>are presented and</sup> nozzle; the results are compared with Sajben's measurements and calculations by other authors.



## SECTION 1 CALCULATION OF VISCOUS FORCES

The momentum equation for unsteady flow in differential form is

$$\frac{\partial \rho \underline{u}}{\partial t} + \nabla \rho \cdot \underline{u} \underline{u} = - \nabla P + \nabla \cdot \mu \nabla \underline{u} + \nabla \cdot \mu \overline{\nabla \underline{u}}^T + \nabla \cdot \delta_{ij} \lambda \frac{\partial u_k}{\partial x_k} \quad (1.1)$$

The normal stresses associated with second coefficient of viscosity,  $\lambda$ , will be neglected in this analysis and in any subsequent calculations. We will be concerned in this section with how the viscous terms ( $\nabla \cdot \mu \nabla \underline{u}$  and  $\nabla \cdot \mu \overline{\nabla \underline{u}}^T$ ) are evaluated using the non-orthogonal, physical mesh system that is incorporated in the present method.

In a control volume analysis of a flow field, we are interested in the actual forces which act upon the control surfaces and the components of these force in the coordinate directions (  $x, y$ , and  $z$  ) rather than the derivatives of the shear stresses as seen in Eq. 1.1. To transform the governing equations from differential form (Eq. 1.1) into an integral form, we use Gauss' theorem. In terms of some arbitrary vector,  $\underline{\phi}$ , Gauss' theorem says,

$$\iiint \nabla \cdot \underline{\phi} dVol = \iint \underline{\phi} \cdot \underline{n} dA \quad (1.2)$$

The viscous terms ( $\nabla \cdot \mu \nabla \underline{u}$  and  $\nabla \cdot \mu \overline{\nabla \underline{u}}^T$ ) in Eq. 1.1, are converted from differential form to control volume form using Eq. 1.2 and the result is,

$$\iiint (\nabla \cdot \mu \nabla \underline{u} + \nabla \cdot \mu \overline{\nabla \underline{u}}^T) dVol = \iint (\mu \nabla \underline{u} \cdot \underline{n} + \mu \overline{\nabla \underline{u}}^T \cdot \underline{n}) dA \quad (1.3)$$

The current two-dimensional scheme uses control volumes which are made up of four straight line segments ( see Fig. 1.1 ). The surface integral in Eq. 1.3 is simplified into a summation over the four sides of the control volume. The integral over the surface in Eq. 1.3 can therefore be represented as

$$\iint (\mu \nabla \underline{u} \cdot d\underline{A} + \mu \overline{\nabla \underline{u}^T} \cdot d\underline{A}) = \sum_{K=1}^4 (\underline{A}_K \cdot \mu \nabla \underline{u} + \underline{A}_K \cdot \mu \overline{\nabla \underline{u}^T}) \quad (1.4)$$

Each area vector in Eq. 1.4 is assigned a magnitude equal to the area of the face in question and a direction which points in the outward normal direction. The evaluation of Eq. 1.4 results in the net viscous forces in the x and y directions for a control volume.

For laminar flow, the absolute viscosity  $\mu$ , is used in Eq. 1.4 to evaluate the shear forces. For turbulent flow, an effective viscosity is used in Eq. 1.4. The effective viscosity that is used is the sum of the absolute viscosity and an apparent eddy viscosity. The current method uses a Prandtl mixing length model to evaluate this eddy viscosity. This mixing length model is outlined in Table 1.1. The details of this mixing length calculation will be presented in section 1.3.

The velocity gradients,  $\nabla u_L$ , needed in Eq. 1.4 can be determined within a non-orthogonal grid by using,

$$\nabla u_L = \frac{\underline{D}_J \times \underline{D}_K}{\underline{D}_I \cdot (\underline{D}_J \times \underline{D}_K)} \frac{\partial u_L}{\partial I} + \frac{\underline{D}_K \times \underline{D}_I}{\underline{D}_J \cdot (\underline{D}_J \times \underline{D}_K)} \frac{\partial u_L}{\partial J} + \frac{\underline{D}_I \times \underline{D}_J}{\underline{D}_K \cdot (\underline{D}_J \times \underline{D}_K)} \frac{\partial u_L}{\partial K} \quad (1.5)$$

where  $\underline{D}_I$ ,  $\underline{D}_J$ , and  $\underline{D}_K$  are directional vectors along the grid directions (I, J, and K), see Appendix A. For the two-dimensional case,  $\partial u_L / \partial K = 0$  and  $\underline{D}_K$  is a vector spanning the height of the duct (in the direction  $\underline{D}_I \times \underline{D}_J$ ). Two typical two dimensional control volumes are shown in Fig. 1.2. The directional vectors ( $\underline{D}_I$  and  $\underline{D}_J$ ) are identified in Fig. 1.2. The magnitudes of the vectors are dependent upon the grid spacing as can be seen in Fig. 1.2. The directional vectors that are shown in Fig. 1.2 would be used to calculate the velocity gradients applicable to the boundary common to both of the control volumes.

The derivatives of the velocities in Eq. 1.5 are taken with respect to the grid indices, in other words,

Table 1.1 Prandlt Mixing Length Viscosity Model

$$\mu_{eff} = \mu_l + \mu_\tau \quad (1)$$

$$\mu_\tau = \rho L^2 \frac{du}{dy} \quad (2)$$

$L$  is the smaller of

0.08 times the width of the boundary layer

0.41 times the distance to the nearest wall

Van Driest Correction

$$L = 0.41 y (1 - \exp[-y \sqrt{\rho \tau} / 26 \mu_l]) \quad (3)$$

Near Wall Correction

$$\mu_{eff} = \sqrt{\mu_l (\mu_l + \mu_\tau)} \quad (4)$$

$$\frac{\partial u_L}{\partial I} = (u_L)_{I+1} - (u_L)_I \quad (1.6)$$

where  $(u_L)_I$  is the velocity at the beginning of vector  $\underline{D}_I$  and  $(u_L)_{I+1}$  is the velocity at the end of vector  $\underline{D}_I$ . For the geometries and boundary conditions investigated in the present work, the gradients in properties in the I direction are much smaller than gradients in the J direction. As a consequence, only the J derivative contributions to Eq. 1.5 will be considered in the present work.

### 1.1 FORCES ON THE SOUTH FACE OF A CONTROL VOLUME

In the actual calculations, for a non-uniform , non-orthogonal grid, the directional vectors are slightly different than those shown in Fig. 1.2. For the south face of a control volume, the area and directional vectors actually used are shown in Fig. 1.3. The directional vector  $\underline{D}_I$ , and the velocity change are evaluated using the downstream nodal values because their use strengthens the centerpoint coefficient of the matrix of unknown variables. The directional vector  $\underline{D}_I$ , is located midway between the four nodes rather than at the boundary surface. This is because the viscosity and velocity gradient used in calculating the shear forces on the south face are evaluated midway between the two nodes. The shear stress is known to vary less through the boundary layer than the velocity gradient or the mixing length squared. Therefore, it is preferable to calculate the shear stress using a velocity gradient and mixing length midway between the grid points in the J-direction and then assign the resulting shear force to the face of the control volume between the points. The upper wall and lower wall control volumes are shown in Figs. 1.4 and 1.5 , respectively with the directional vectors identified. The shear stresses are evaluated midway between the wall and the near wall point and then the shear forces are assigned to the wall surface. The effective viscosity used to evaluate these wall shear forces is a combination of the laminar and turbulent viscosities given by

$$\mu_{eff} = \sqrt{\mu(\mu_l + \mu_t)} \quad (1.7)$$



This relationship is used only at the wall and has been shown ( Ref. 4 ) to allow a good calculation of wall shear stress with a near wall point further away from the wall than is typically required.

Symmetry is used to calculate the forces on the north face of a control volume, in other words,

$$\vec{F}_{north,I,J} = - \vec{F}_{south,I,J+1} \quad (1.8)$$

where  $\vec{F}_{north}$  and  $\vec{F}_{south}$  are the shear forces on the north and south faces of the control volume respectively.

## 1.2 FORCES ON THE WEST FACES OF A CONTROL VOLUME

The forces on the west face of the control volume are calculated by scalar multiplying an interpolated shear stress with the west face area vector ( see Eq. 1.4 ). Referring to Fig. 1.6, for a node point (I,J) which is located on the west face of control volume (I,J), first the velocity gradient and viscosity are calculated at the western edge of surfaces A and B which are midway between the node points (I,J) and (I,J-1) and node points (I,J+1) and (I,J), respectively. The west sides of surfaces A and B are also the locations where the shear stresses are calculated for the north and south faces of the control volume (I-1,J). The product of the velocity gradient and viscosity at node ( I,J ) is determined by linearly interpolating using the following interpolation formula,

$$\phi_{I,J} = \phi_A + \frac{(y_A/2)}{(\frac{y_B}{2} + \frac{y_A}{2})} (\phi_B - \phi_A) \quad (1.9)$$

where  $\phi_A$  and  $\phi_B$  are the products of the velocity gradient and the viscosity at the west sides of surfaces A and B respectively. Once these interpolated values have been calculated, Eq. 1.4 can be used to calculate the components of the shear forces on the west face. The shear stress is interpolated to node I,J rather than interpolating the velocity gradient since the shear stress varies less through the boundary layer than the velocity gradient. Similarly for the east face we have

$$\vec{F}_{east,I,J} = - \vec{F}_{west,I+1,J} \quad (1.10)$$

### 1.3 CALCULATION OF MIXING LENGTH AND VISCOSITY

When the mixing length model of Table 1.1 is used in the 0.41y region, a distance normal to the wall, "y", must be determined to calculate the mixing length. For a flat wall, the distance to the wall from a point is, of course, measured along a line perpendicular to the wall. However, with the current grid system, grid lines and lines orthogonal to the wall are not coincident ( see Fig. 1.7 ). Fig. 1.7 shows 5 adjacent control volumes. The normal distance (L) between the north and south faces of a control volume is equal to the volume of the control volume divided by the distance (S) between the east and west faces of the control volume measured in the I grid direction. The total normal distance from the wall to the node point on the west face of a control volume (  $L_{west}$  ) is equal to the sum of all previous normal distances between that control volume and the nearest wall plus one half of the normal distance for that control volume. We can represent that distance as

$$L_{west} = \sum_{k=1}^{n-1} L_k + 0.5 \times L_n \quad (1.11)$$

where n is the number of control volumes from the wall.

The total normal distance needed for calculating the mixing length for the south face of a control volume (  $L_{south}$  ) is equal to the sum of all previous normal distances to the previous node (  $L_{west,n-1}$  ) plus the equivalent normal distance half way between the two grid points in question. The procedure used to calculate this length is shown in Fig. 1.8. We can represent this total distance as

$$L_{south,n} = L_{west,n-1} + \frac{(L_{n-1} + L_n)}{4} \quad (1.12)$$

To determine the mixing length in the outer part of the boundary layer, the boundary layer thickness measured normal to the wall must also be determined. The lengths that were calculated above can also be used in calculating the boundary layer thickness. The edge of the boundary layer is determined by using the magnitude of the normalized local total pressure gradient as a measure of its location. The normalized total pressure gradient used here is

$$\text{normalized total pressure gradient} = \frac{\Delta P_t}{\Delta y} \frac{1}{0.5 \rho_e u_e^2} \quad (1.13)$$

where " $\Delta y$ " is the normal distance between two grid points. The local freestream values of density and velocity are used in Eq. 1.13. The grid line that is considered the freestream is input into the method. Starting from the freestream the normalized total pressure gradient ( Eq. 1.13 ) is calculated between grid points and is compared with a characteristic normalized total pressure gradient. The edge of the boundary layer is defined as where the magnitude of the calculated gradient is equal to the characteristic gradient. The exact distance is determined using interpolation and is based upon the distances normal to the wall. The characteristic normalized total pressure gradient is determined by

$$\frac{\Delta P_{t, \text{char}}}{\Delta y} \frac{1}{0.5 \rho_e u_e^2} = \frac{1}{CL} \quad (1.14)$$

where CL is some characteristic length of the flow field, typically the duct width.

Once the mixing length has been calculated, the apparent eddy viscosity is calculated using Eq. 1 in Table 1. The velocity gradient used in the eddy viscosity calculation is determined using the following expression,

$$\frac{du}{dy} = \sqrt{\left[ \frac{\underline{A} \cdot \nabla u}{|A|} \right]^2 + \left[ \frac{\underline{A} \cdot \nabla v}{|A|} \right]^2} \quad (1.15)$$

where  $\underline{A}$  is the area vector on the south side of the control volume. This formula gives the magnitude of the total velocity gradient reflecting the non-orthogonality of the grid.

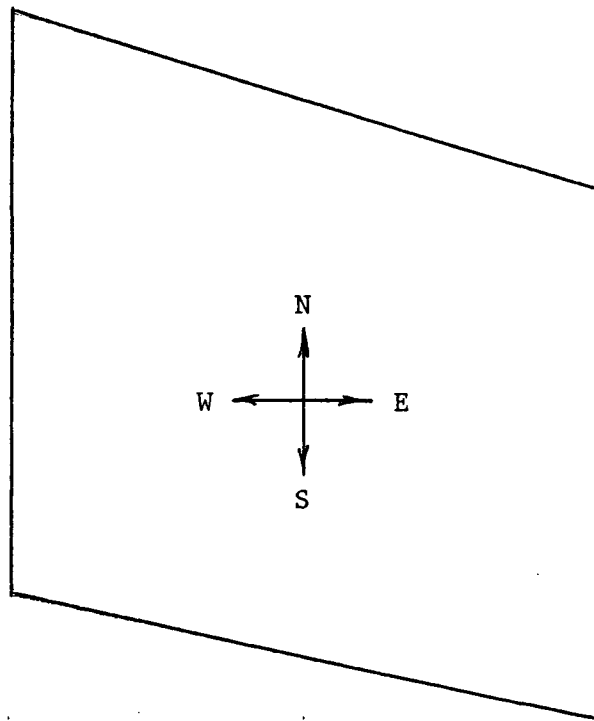


Fig. 1.1 Typical Control Volume

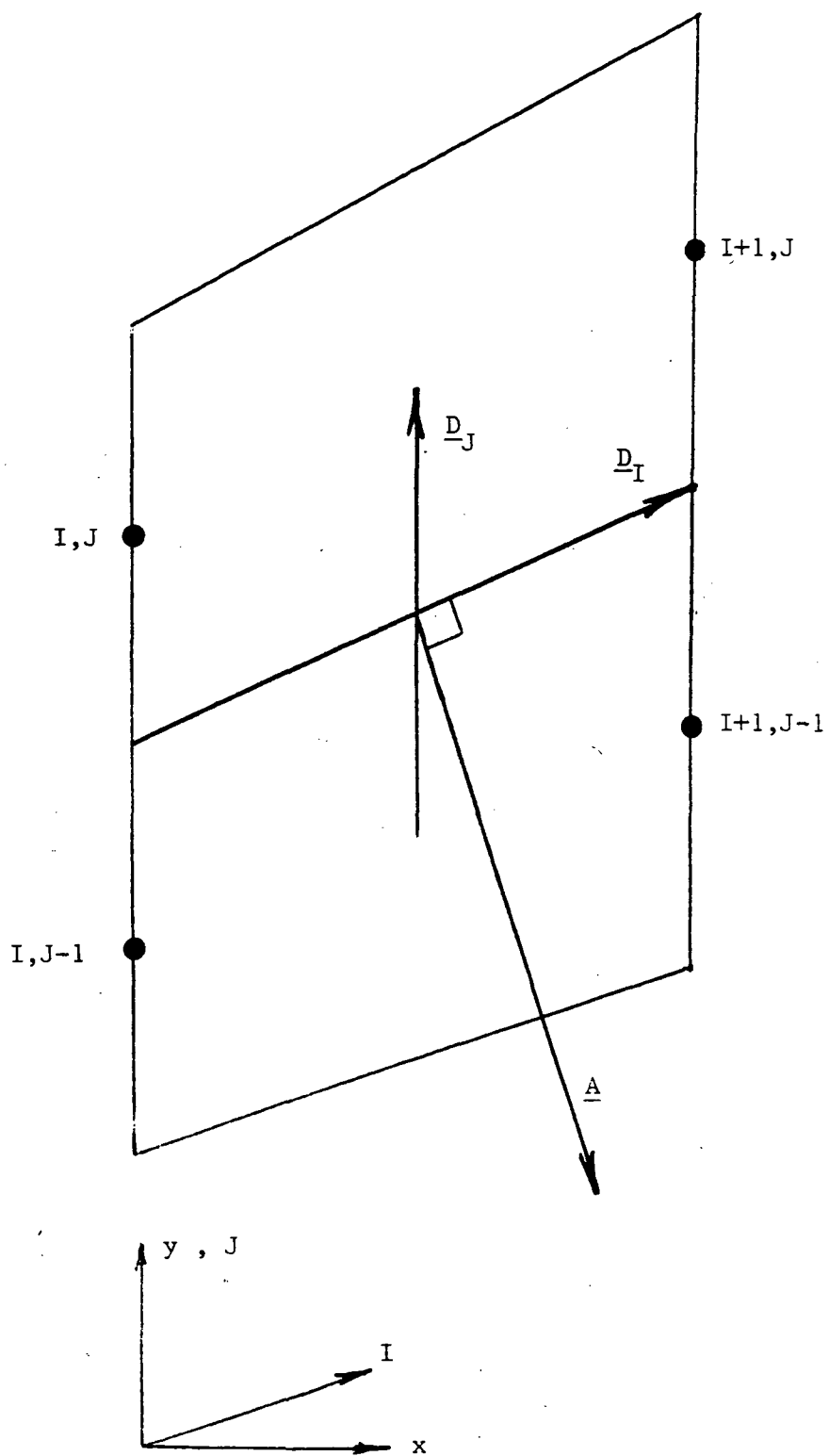


Fig. 1.2 Two Typical Control Volumes

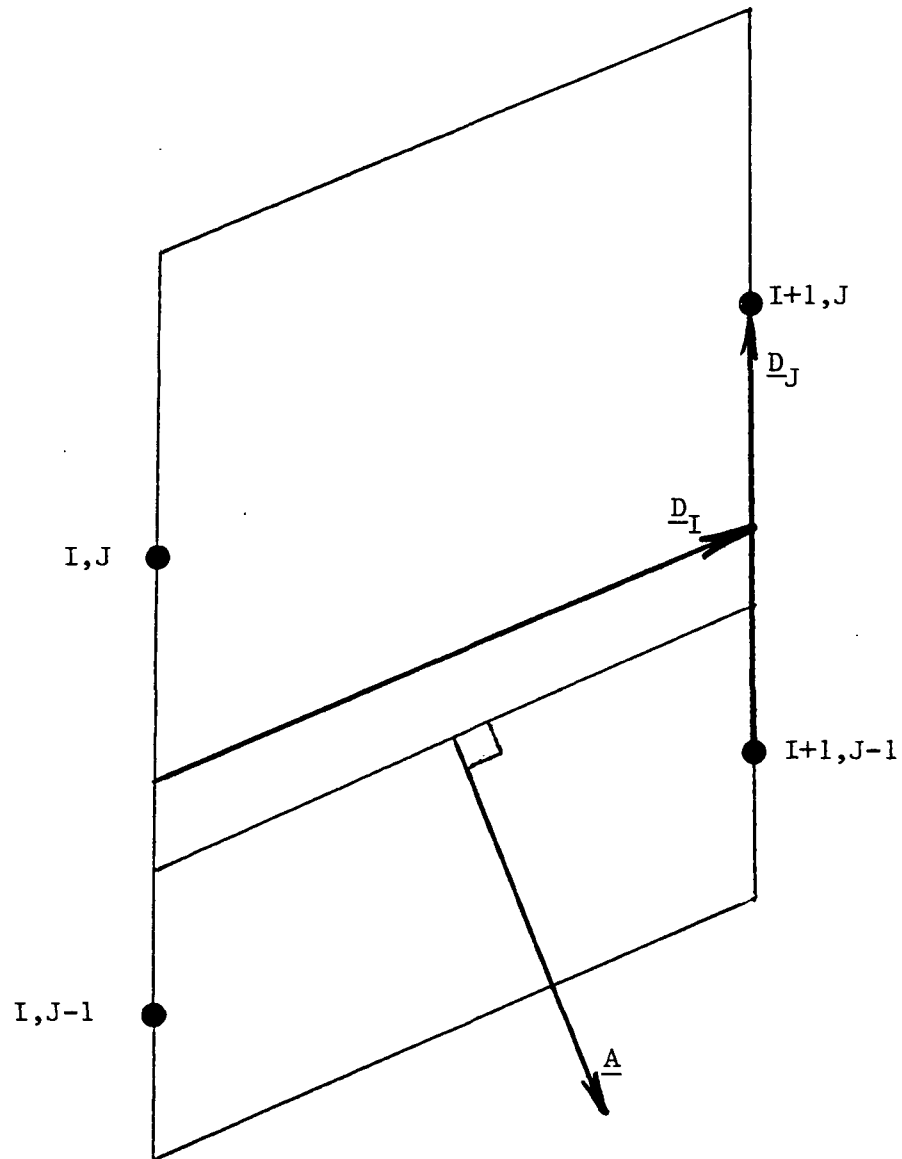


Fig. 1.3 Two Typical Control Volumes With Directional Vectors Identified For South Face



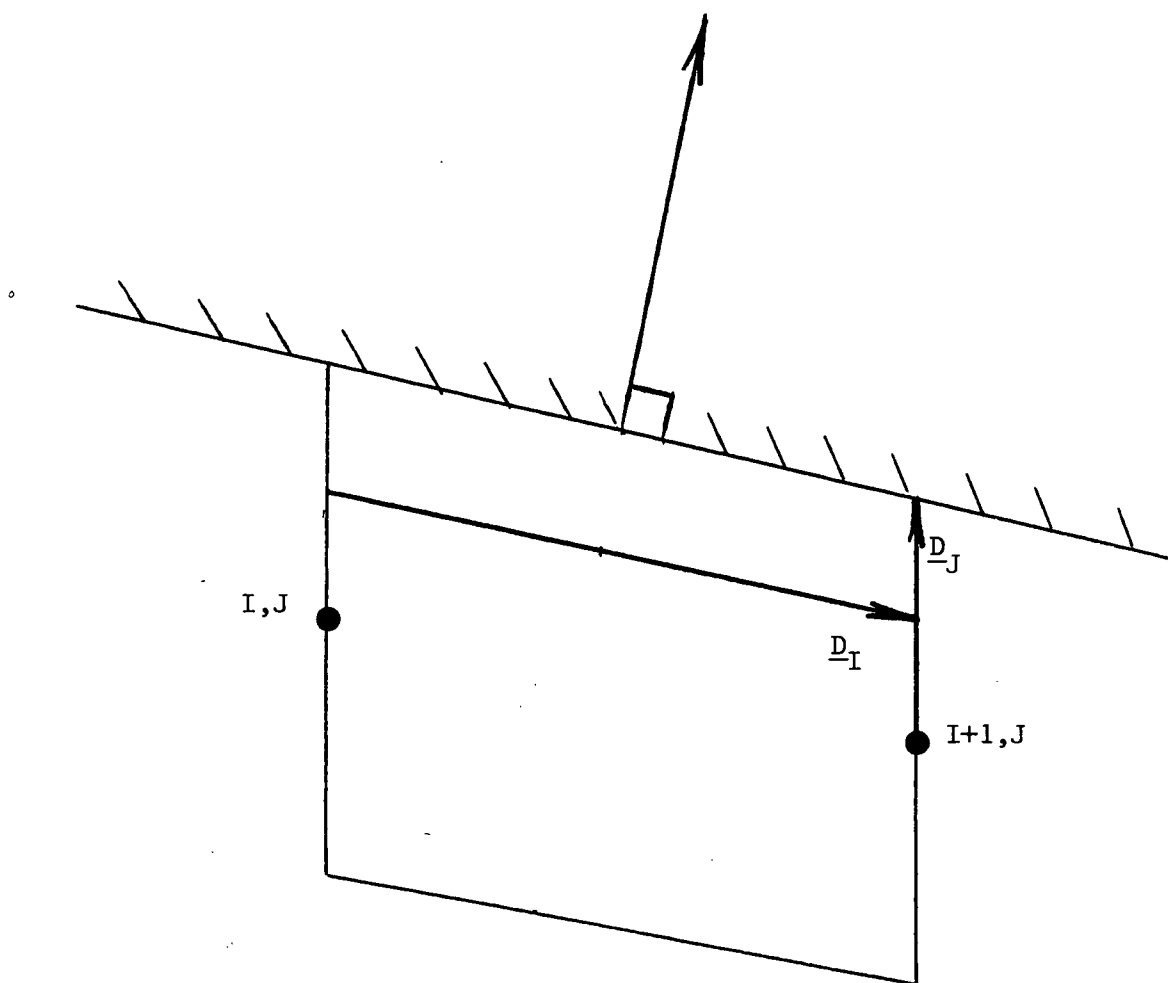


Fig. 1.4 Upper Wall Control Volume

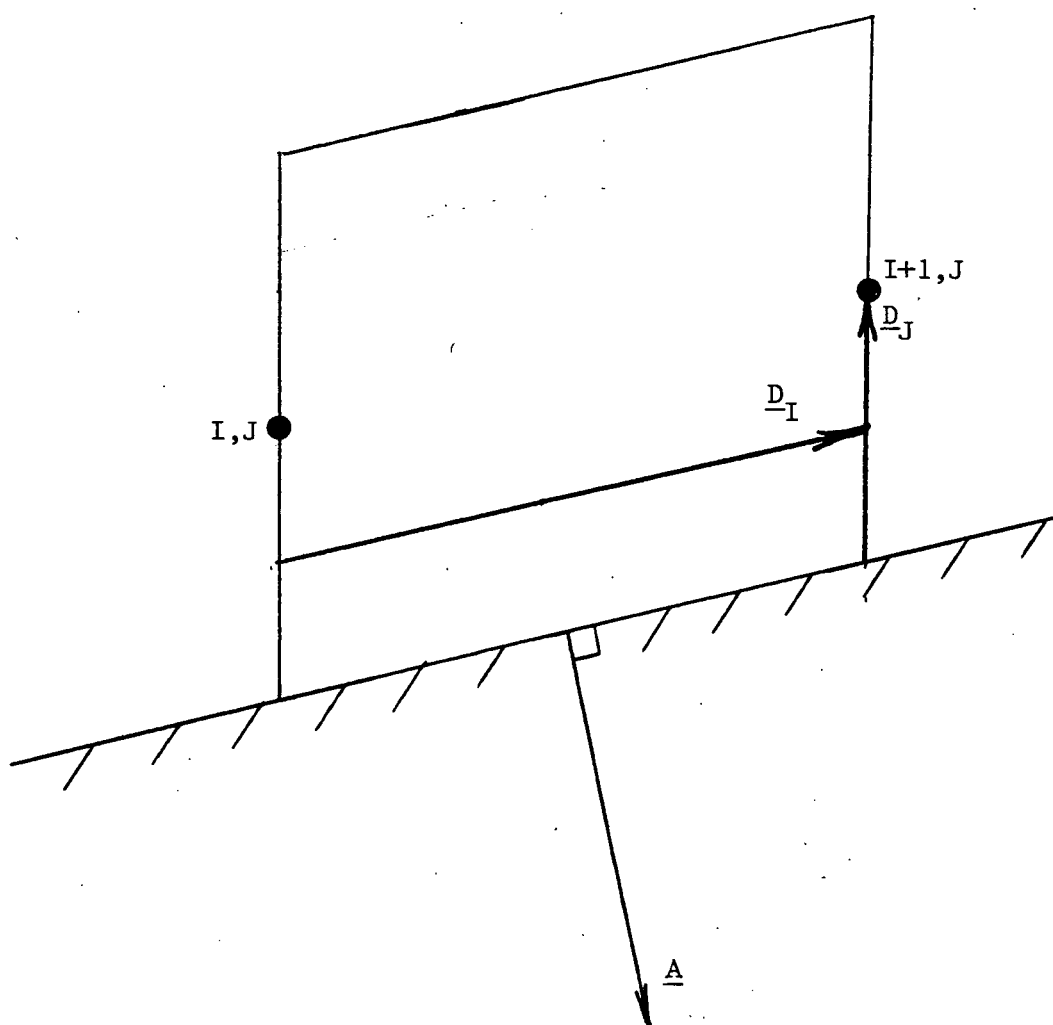


Fig. 1.5 Lower Wall Control Volume

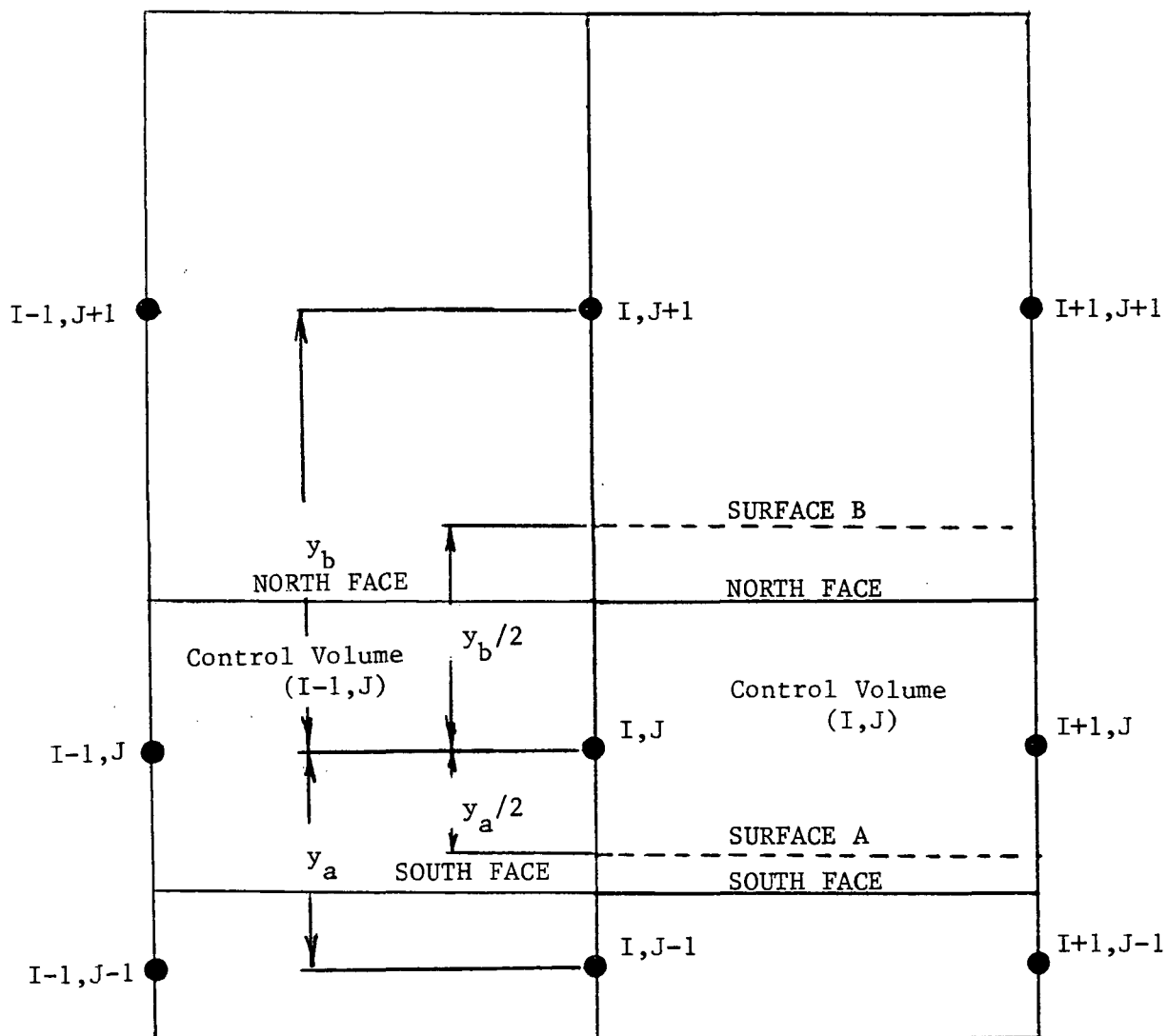


Fig. 1.6 Control Volume Arrangement for West Face Force Evaluation

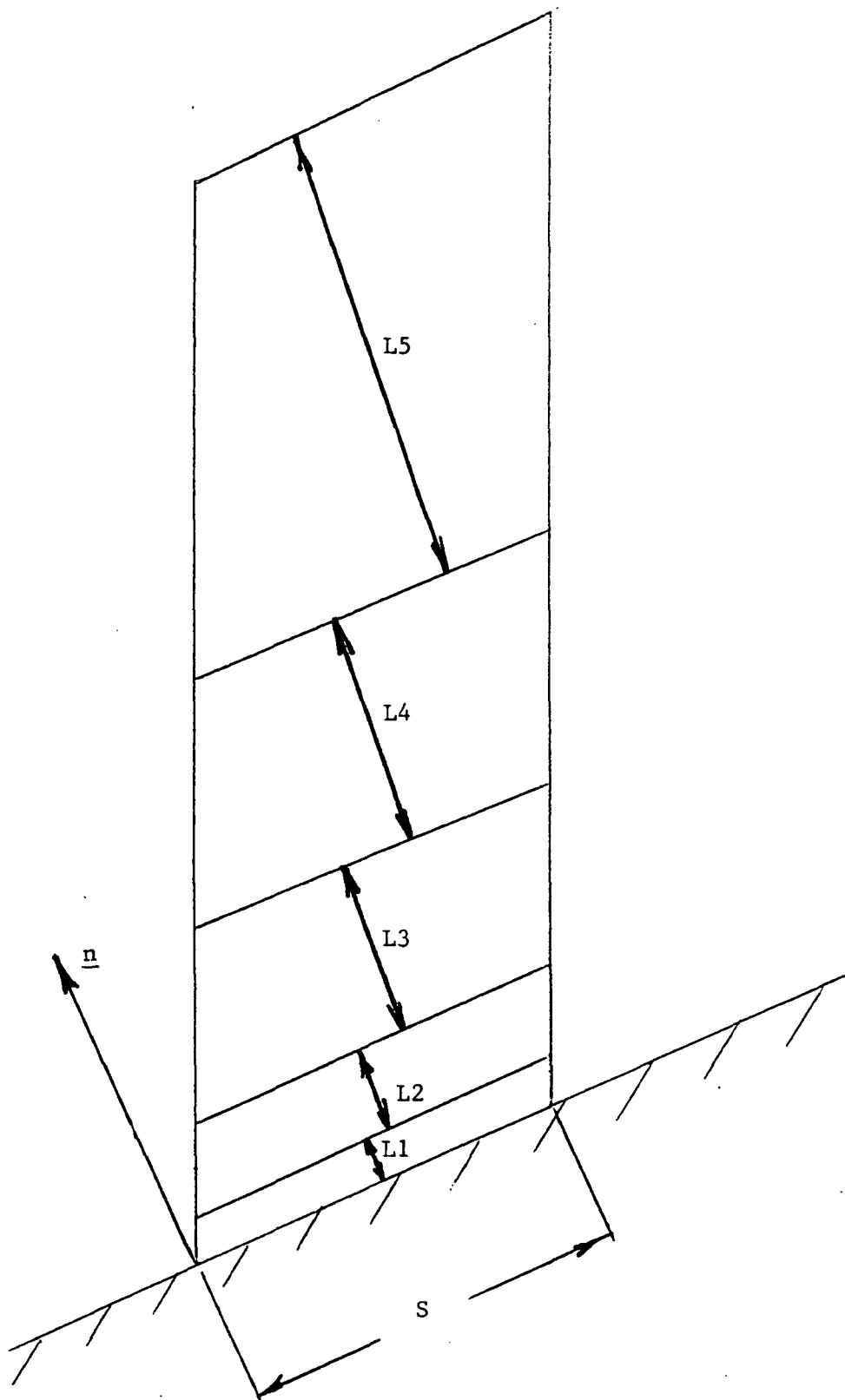


Fig. 1.7 Distances Normal to the Wall

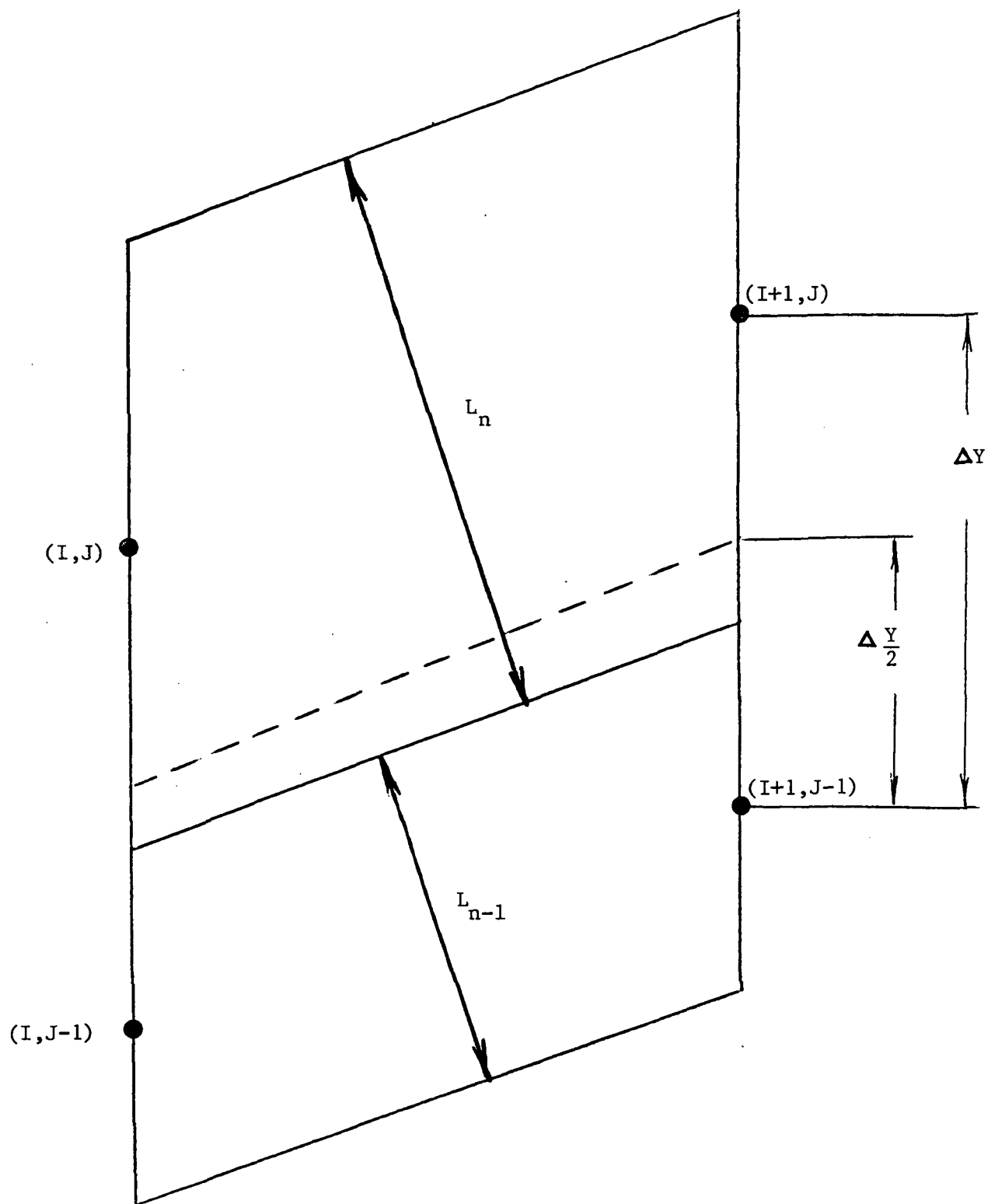


Fig. 1.8 Normal Distance to the South Face of the Control Volume

## SECTION 2 LAMINAR BOUNDARY LAYER IN TWO CONVERGING DUCTS

A laminar boundary layer is calculated on the curved wall of two converging ducts. The other wall is straight and was treated as inviscid in the calculations. In all the calculations, the inlet boundary layer thickness is 5% of the inlet duct height. The inlet velocity profile is the Blasius profile. The inlet height of the duct is 44 mm and the exit height is 31 mm. The length of the duct is 180.4 mm. The absolute viscosity is .001 kg/m s. The inlet freestream Mach number is 0.10.

Two geometries are investigated with the basic dimensions given above. For one geometry, the curved wall radius is determined using a sine wave formulation. This geometry has a smooth transition from the inlet to the exit sections. The second geometry is essentially the same except that the radius is not determined using an analytical function and the second derivative of the wall radius is discontinuous. Both uniform and non-uniform grids are used in the boundary layer region. Figures 2.1 through 2.3 show the grid and geometry for the 3 arrangements to be investigated. The arrangements are

1. Smooth geometry using non-uniform grid ( Fig. 2.1 )
2. Smooth geometry using uniform grid ( Fig. 2.2 )
3. Non-smooth geometry using uniform grid ( Fig. 2.3 )

A plot of the 2nd derivative of the wall radius as a function of axial position for the non-smooth and smooth geometries is seen in Fig. 2.4. The location of the discontinuity is also identified in Fig. 2.3.

The specific ideas which are to be illustrated using this test case are,



1. Comparison of skin friction coefficients calculated using the finite volume method with those calculated using Thwaites method.
2. Comparison of skin friction coefficients calculated using uniform and non-uniform grids.
3. Comparison of skin friction coefficients calculated using smooth and non-smooth geometries.
4. Investigation of pressure variations across the duct comparing the uniform and non-uniform grids results, and non-smooth geometry results.
5. Investigation of inlet and exit boundary condition specifications.
6. Investigation of the convergence properties of uniform vs non-uniform grids, coarse vs fine grids, and different multi-volume approaches.

The radial distribution of grid points for the coarse, uniform and non-uniform grids and the fine non-uniform grid are tabulated in Table 2.1.

For the smooth geometry in Fig. 2.1, the skin friction coefficient along the duct was calculated using the finite volume method and using the method of Thwaites (5). A coarse non-uniform grid was used for the finite volume calculations. Thwaites method is an integral method used to calculate the development of laminar boundary layers in incompressible flow. Using the wall static pressure distribution from the finite volume calculation as a boundary condition, the skin friction coefficient was calculated with Thwaites method. Fig. 2.5 compares the skin friction coefficients obtained from the finite volume calculations with those obtained using Thwaites method. The agreement is good for most of the flow; however, near the exit of the duct there is a discrepancy. This discrepancy may be due to the fact that the boundary layer has grown to over 25% of the duct height at the exit.

Table 2.1 Radial Distribution of Grid Points  
for Laminar Calculations

	Uniform Grid <u>Coarse</u>	Non-Uniform Grid <u>Coarse</u>	Non-Uniform Grid <u>Fine</u>
	y/h	y/h	y/h
P1	.005	.0024	.0004
P2	.015	.0071	.00115
P3	.025	.0142	.00225
P4	.035	.0283	.0040
P5	.045	.0563	.0075
P6	.060	.1125	.0150
P7	.085	.225	.0300
P8	.125	.400	.0575
P9	.200	.625	.1125
P10	.375	.875	.225
P11	.625	-	.400
P12	.875	-	.625
P13	-	-	.875

The skin friction coefficients calculated with the finite volume method using uniform and non-uniform grids are shown in Fig. 2.6. The agreement is excellent and it is concluded that grid spacing does not affect the prediction of the skin friction coefficient for this laminar flow.

The skin friction coefficients for the flow through the smooth and non-smooth geometries are shown in Fig. 2.7. Superficially, the geometries in Figs. 2.2 and 2.3 look almost identical ; however, for the non-smooth geometry the second derivative of the lower wall radius of curvature is discontinuous (see Fig. 2.4) causing the solution to be erratic at the discontinuity. To ensure smooth calculations, geometries input into this program should have continuous second derivatives.

The cause for the rapid increase in the skin friction coefficient at the discontinuity can be seen in Fig. 2.8. Fig. 2.8 is a plot of a transverse pressure coefficient which is defined as

$$C_{Pt} = \frac{p - p_{fs}}{0.5\rho u^2} \quad (2.1)$$

where  $p$  is the local static pressure at an axial location,  $p_{fs}$  is the freestream static pressure at this axial location , and  $0.5\rho u^2$  is the dynamic pressure at the inlet to the nozzle. The different curves in Fig. 2.8 represent the pressure coefficient at every other grid line from the wall to the freestream. Because of curvature, the pressure gradient across the duct first rises and then falls. The wall pressure (  $p_l$  ) is seen to change very rapidly at the point of the discontinuity. This large axial pressure gradient results in a large change in velocity at the discontinuity and thus the large change in skin friction coefficient that was seen in Fig. 2.7.

For the smooth geometry the transverse pressure coefficient is shown in Fig. 2.9. The pressure changes are smooth throughout the entire length of the duct. The pressure coefficients shown in Fig. 2.9 are from calculations using a non-uniform grid. Fig. 2.10 shows identical results for calculations made using a uniform grid in the boundary layer.

In Figs. 2.8, 2.9, and 2.10, a small transverse pressure gradient can be observed at the inlet to the duct. This small transverse pressure gradient is a result of specifying the inlet v-velocity to be equal to zero. This boundary condition would be typical of inviscid calculations ; however, the boundary layer in this viscous flow does have a finite v-velocity as a result of the growth of the boundary layer. The growth of the boundary layer for this test case is large because of the high absolute viscosity used. An additional calculation was made by modifying the boundary condition on the inlet v-velocity. From a previous calculation, the flow angles at the second axial station were recorded. These flow angles were then used as the inlet boundary condition for the inlet flow angle in a subsequent calculation. The transverse pressure coefficients for this case are shown in Fig. 2.11. The inlet transverse pressure coefficient is reduced considerably when compared with the pressure coefficient shown in Fig. 2.9. When the Blasius solution was used to calculate the inlet v-velocity distribution, the solution over compensated and the transverse pressure gradient was in the opposite direction to that calculated when a zero v-velocity was specified.

It was also found to be important that the inlet and exit lengths of the straight portions of the duct were long enough. Oscillations in the static pressure would occur at the inlet and exit if these lengths were too short.

An additional pressure coefficient was calculated for each of the cases described above. The pressure coefficient is defined as

$$C_p = \frac{p_{01} - p}{0.5\rho u^2} \quad (2.2)$$

where  $p_{01}$  is the freestream total pressure,  $p$  is the local static pressure, and  $0.5\rho u^2$  is the inlet dynamic pressure. This pressure coefficient again shows the effect of curvature on the pressure through the boundary layer but it also shows the relative acceleration of the flow through the nozzle. The plots are

1. non-smooth geometry with uniform grid ( Fig. 2.12 )

2. smooth geometry with non-uniform grid ( Fig. 2.13 )
3. smooth geometry with uniform grid ( Fig. 2.14 )
4. inlet flow angle specified with non-uniform grid ( Fig. 2.15 )

This test case also provided us with an opportunity to investigate the stability and convergence properties of various multi-volume approaches (2) within the boundary layer. The various strategies are

1. [MV1] no multi-volume used in a uniform grid
2. [MV2] multi-volume used in a uniform grid with time steps based upon properties for the individual control volume farthest away from the wall.
3. [MV3] multi-volume used in a uniform grid with time steps based upon average properties for the entire multi-volume region.
4. [MV4] multi-volume used in a non-uniform grid with time steps based upon properties for the individual control volume farthest away from the wall.
5. [MV5] multi-volume used in a non-uniform grid with time steps based upon average properties for the entire multi-volume region.

For the uniform and non-uniform grids, the multivolume approach was used for the 6 control volumes nearest to the wall.

Two measures of convergence will be used in the following analysis. The maximum change in velocity in the flow field for one iteration divided by an average velocity for the flow field all multiplied by the time factor used in the time step determination will be our momentum residual, in other words,

$$\text{momentum residual} = \frac{(u^{n+1} - u^n)_{\max}}{u_{\text{avg}}} \times \text{TIMEF} \quad (2.3)$$

The time factor, TIMEF, is included so that calculations using different time factors in the time step determination can be judged on a common basis. A time factor of 4.0 was used for all of the laminar calculations. The mass flow rate error is defined as

$$\text{mass flow error} = \left| \frac{\dot{m}_{\text{local}} - \dot{m}_{\text{in}}}{\dot{m}_{\text{in}}} \right|_{\max} \times 100 \quad (2.4)$$

The momentum residual for multi-volume approaches 1 through 4 are shown in Fig. 2.16. The mass flow error for approaches 1 through 4 are shown in Fig. 2.17. The non-uniform grid shows superior convergence properties when compared with the uniform grid results. When the uniform grid is used, approach MV3 is the best.

When the momentum residual and mass flow error for the non-uniform grid approaches MV4 and MV5 are compared in Figs. 2.18 and 2.19, the results are very similar. This agreement justifies the use of the simpler multi-volume approach ( MV4 ) for the non-uniform grid. The simpler multi-volume approach uses less computer time in the multi-volume part of the program.

When a finer grid was used with the non-uniform grid arrangement in the boundary layer region ( twice as many control volumes ), the skin friction coefficients were identical to those calculated from the coarse grid ( 5 points in the boundary layer). The momentum residual and the mass flow error for the coarse and fine grids are compared in Figs. 2.20 and 2.21 respectively. The convergence properties are very similar.

The following conclusions can be reached from the above test case:



- a. the geometries should be inspected for discontinuities in the second derivative to ensure smooth solutions.
- b. uniform and non-uniform grids give essentially identical results for this laminar boundary layer.
- c. the non-uniform grid (with a factor of 2 change in spacing) has superior convergence properties.
- d. the simple form of the multi-volume used with the non-uniform grid (MV4) is preferred because of the reduced computational effort required.

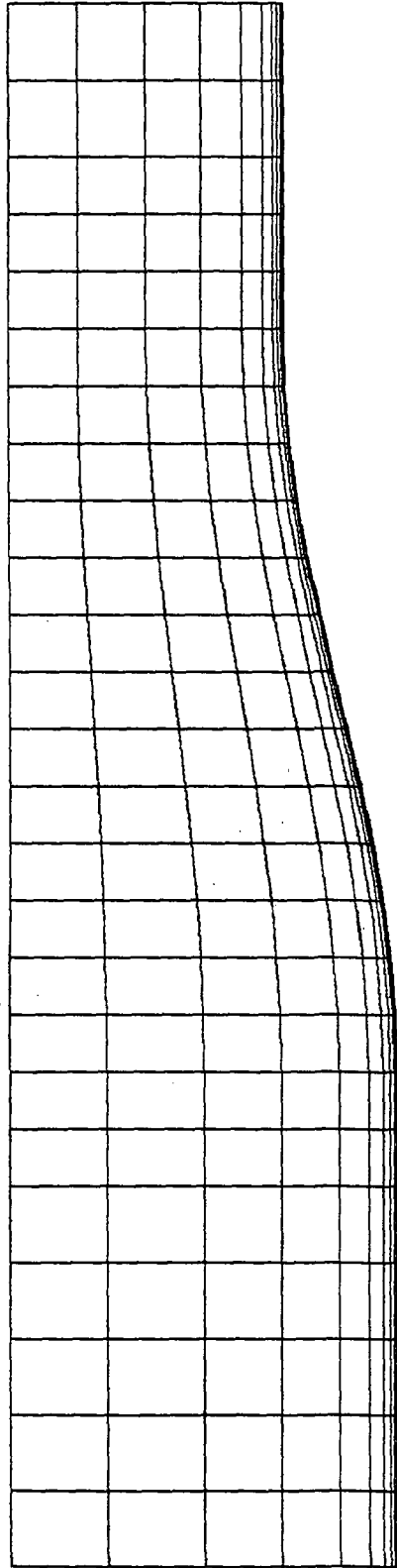


Fig. 2.1 Smooth Geometry Using Non-Uniform Grid

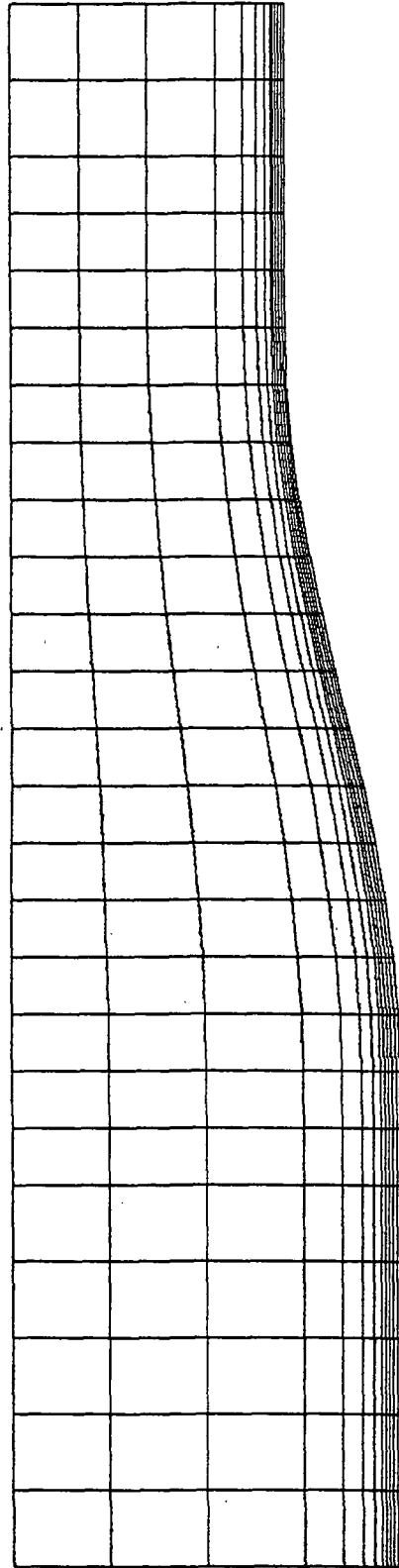


Fig. 2.2 Smooth Geometry Using Uniform Grid

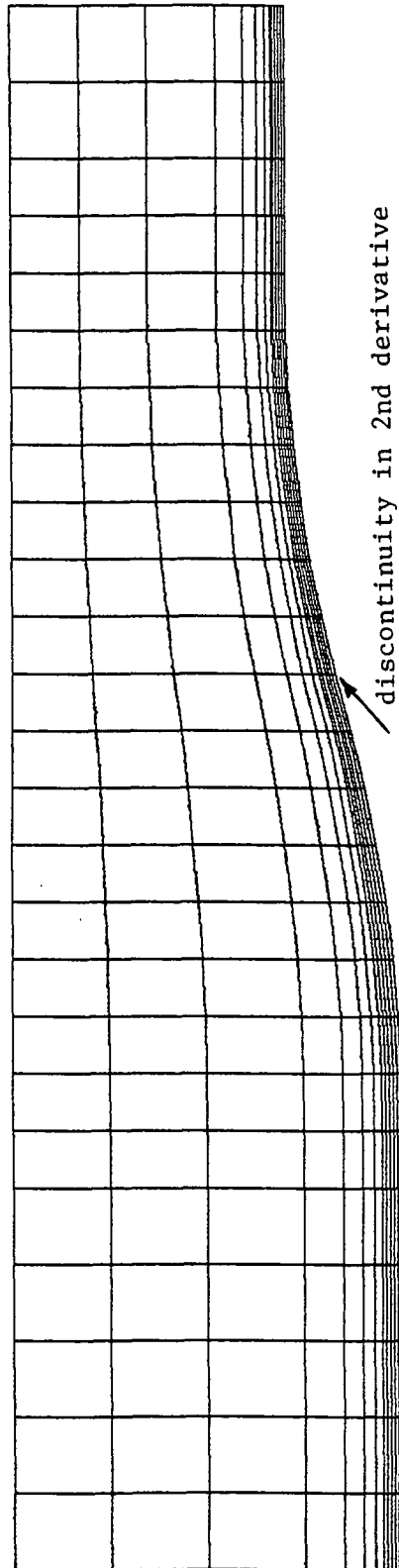


Fig. 2.3 Non-Smooth Geometry Using Uniform Grid

FIG. 2.4 SECOND DERIVATIVE OF RADIUS  
FOR CONVERGING DUCT

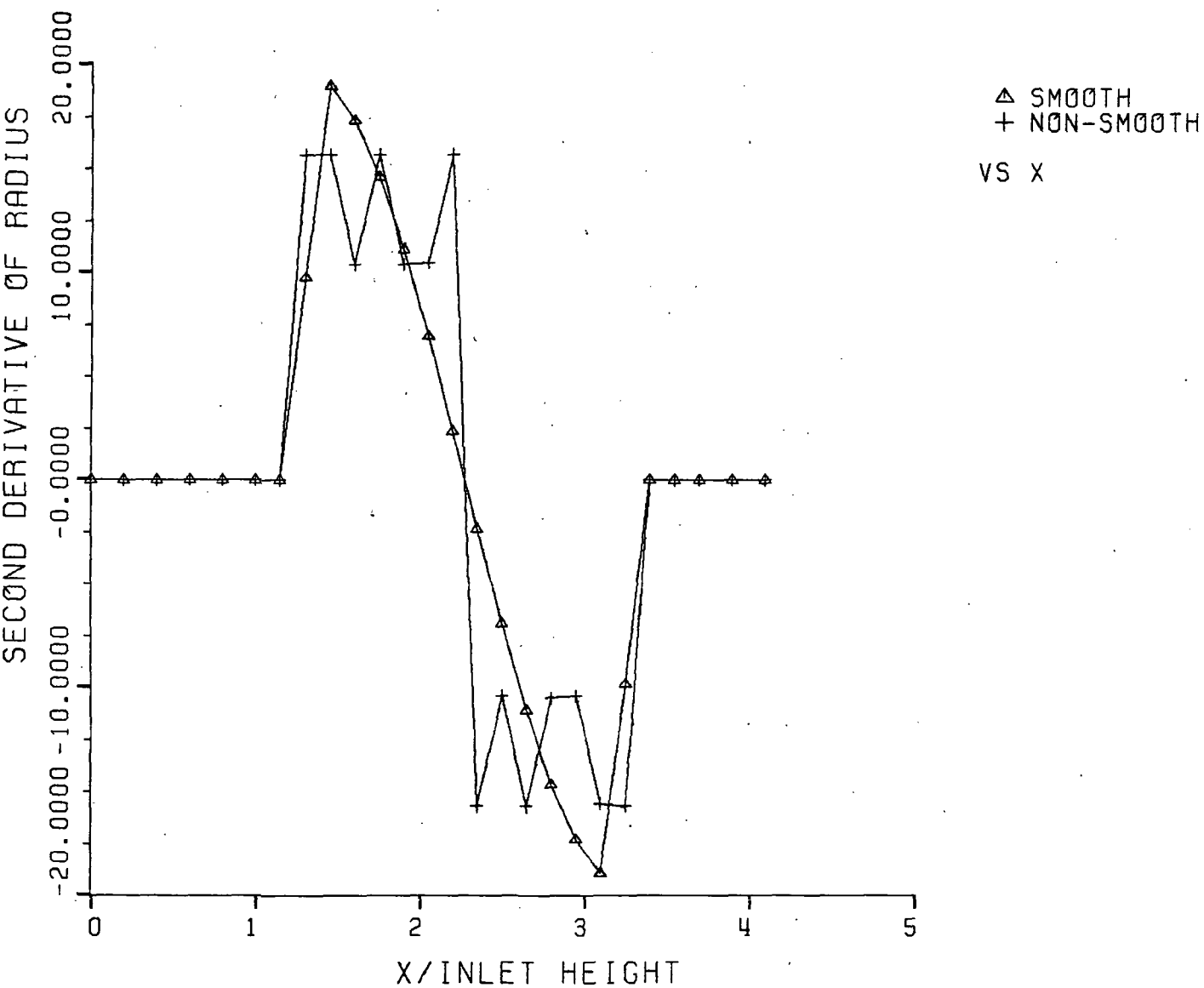


FIG. 2.5 SKIN FRICTION COEFFICIENT  
FINITE VOLUME METHOD  
VS THWAITES METHOD

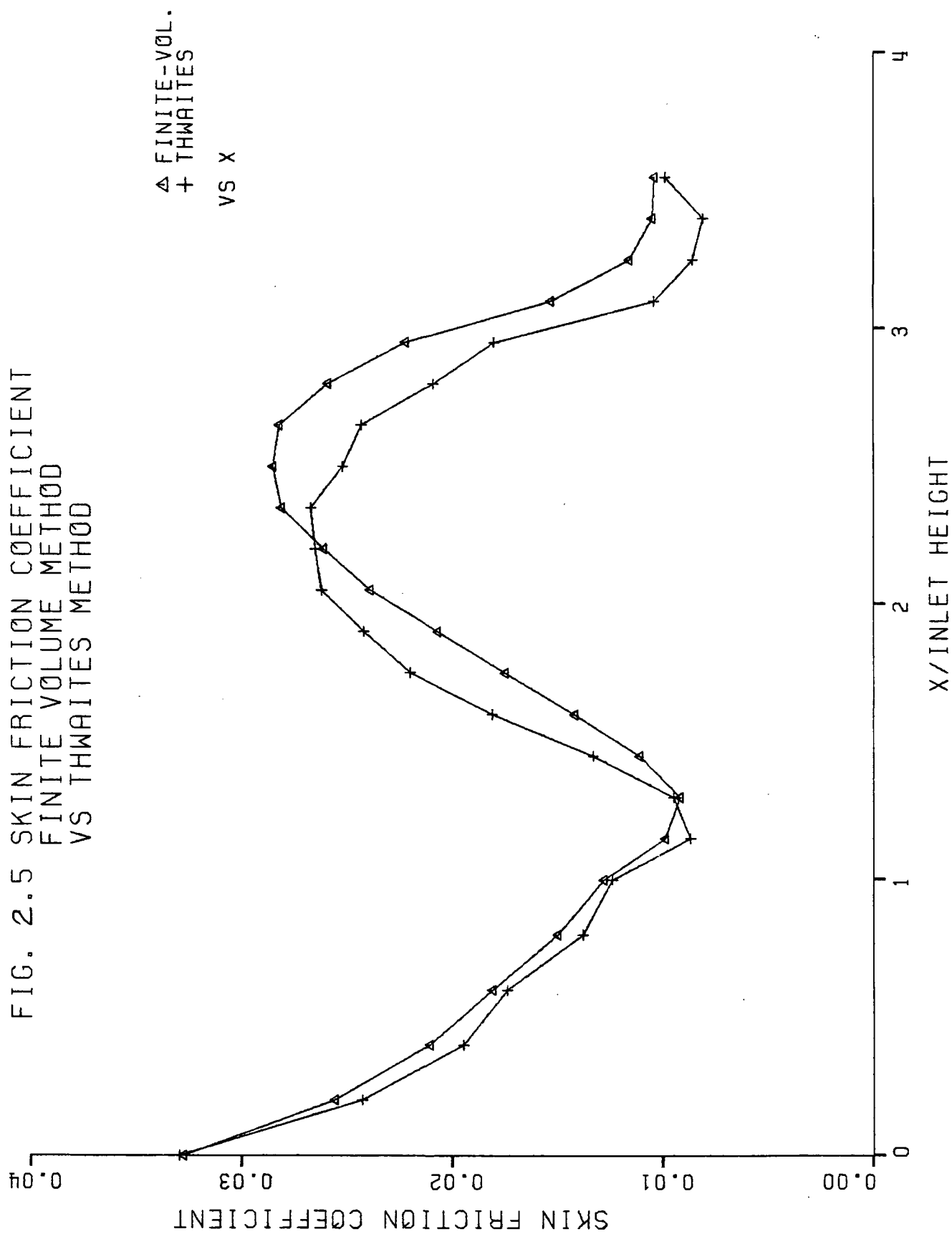




FIG. 2.6 SKIN FRICTION COEFFICIENT  
FINITE VOLUME METHOD  
NON-UNIFORM VS UNIFORM GRIDDING

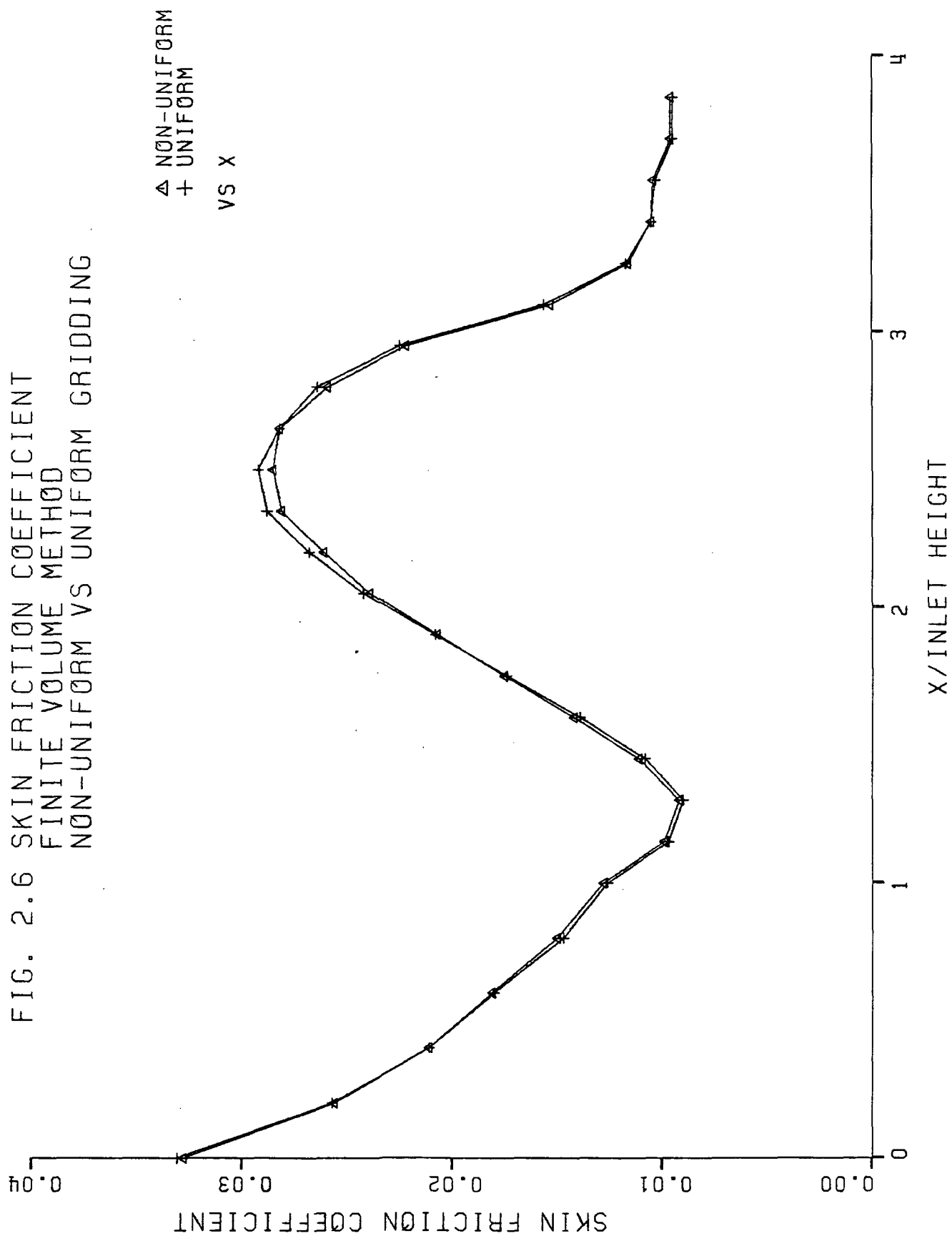


FIG. 2.7 SKIN FRICTION COEFFICIENT  
SMOOTH GEOMETRY VS  
NON-SMOOTH GEOMETRY

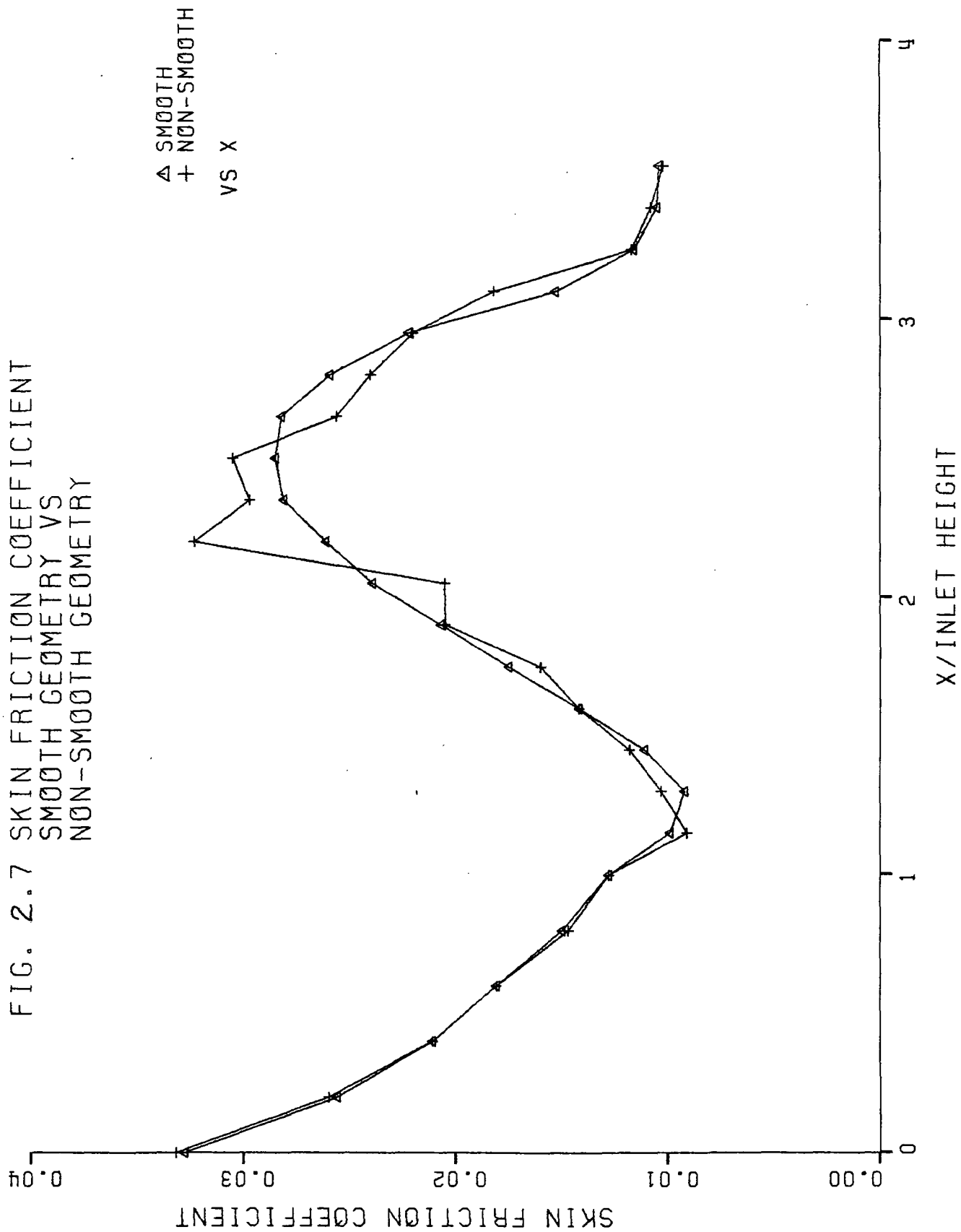


FIG. 2.8 TRANSVERSE PRESSURE COEFFICIENT  
NON-SMOOTH GEOMETRY UNIFORM GRID

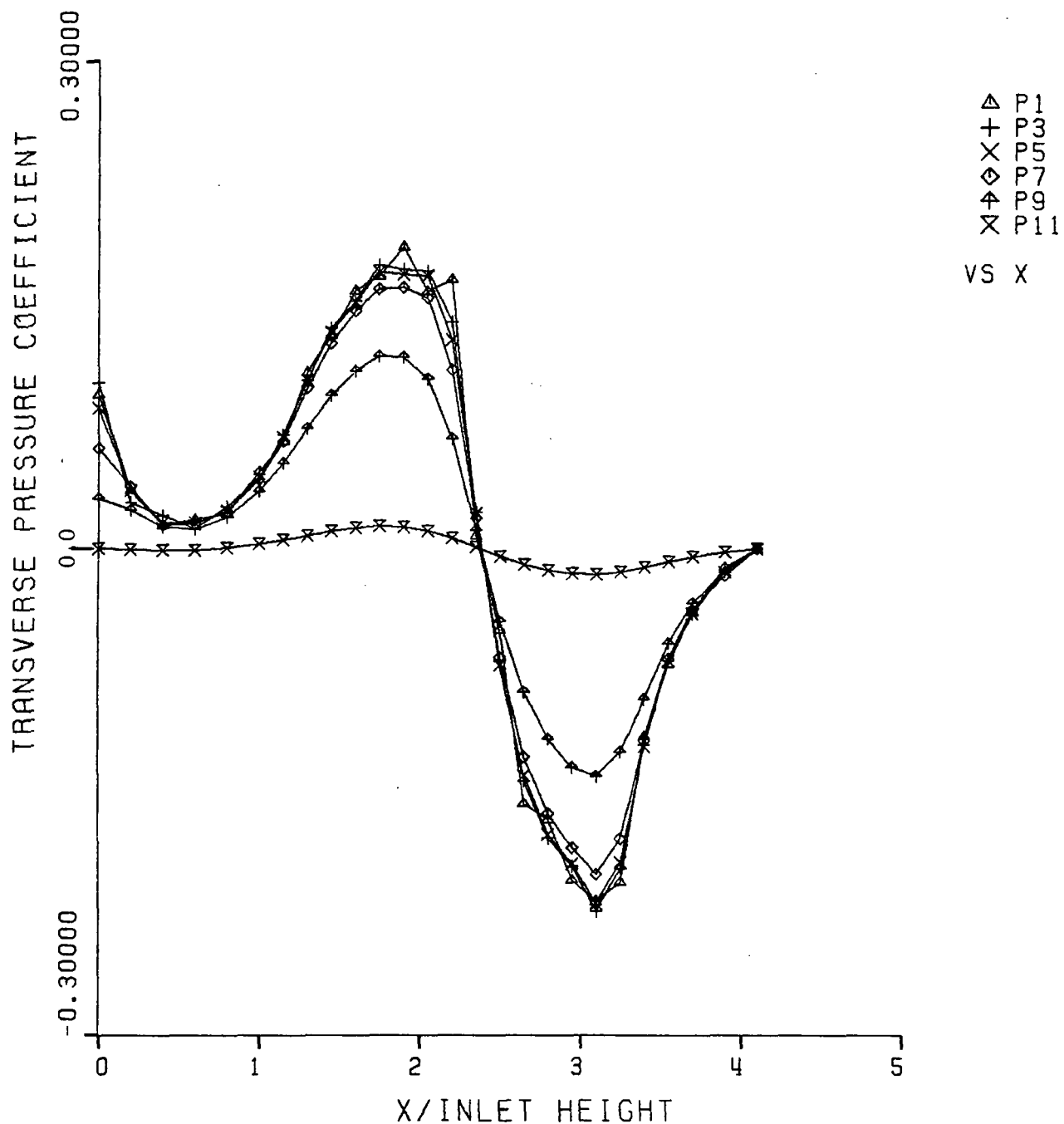


FIG. 2.9 TRANSVERSE PRESSURE COEFFICIENT  
SMOOTH GEOMETRY NON-UNIFORM GRID

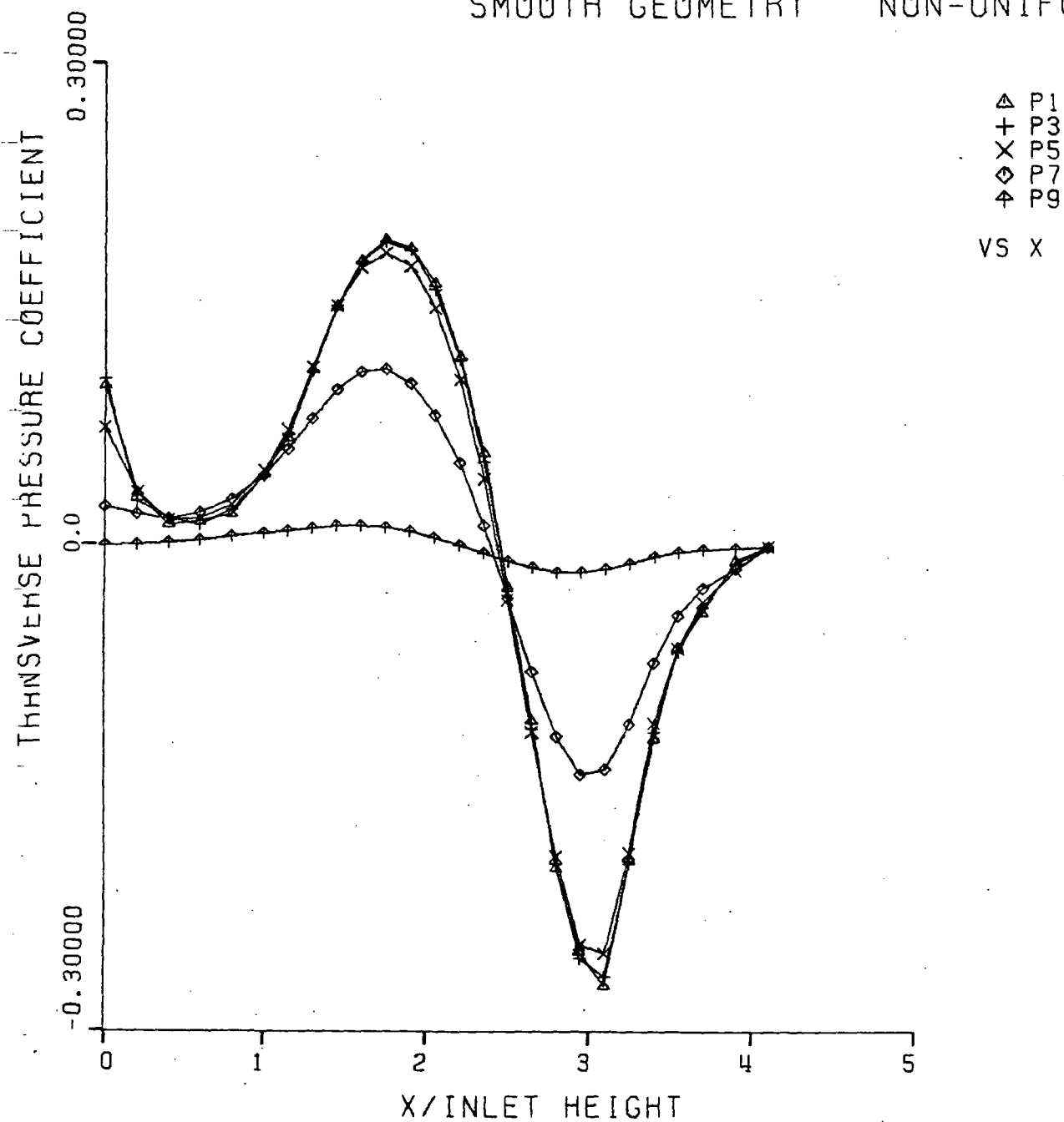


FIG. 2.10 TRANSVERSE PRESSURE COEFFICIENT  
SMOOTH GEOMETRY UNIFORM GRID

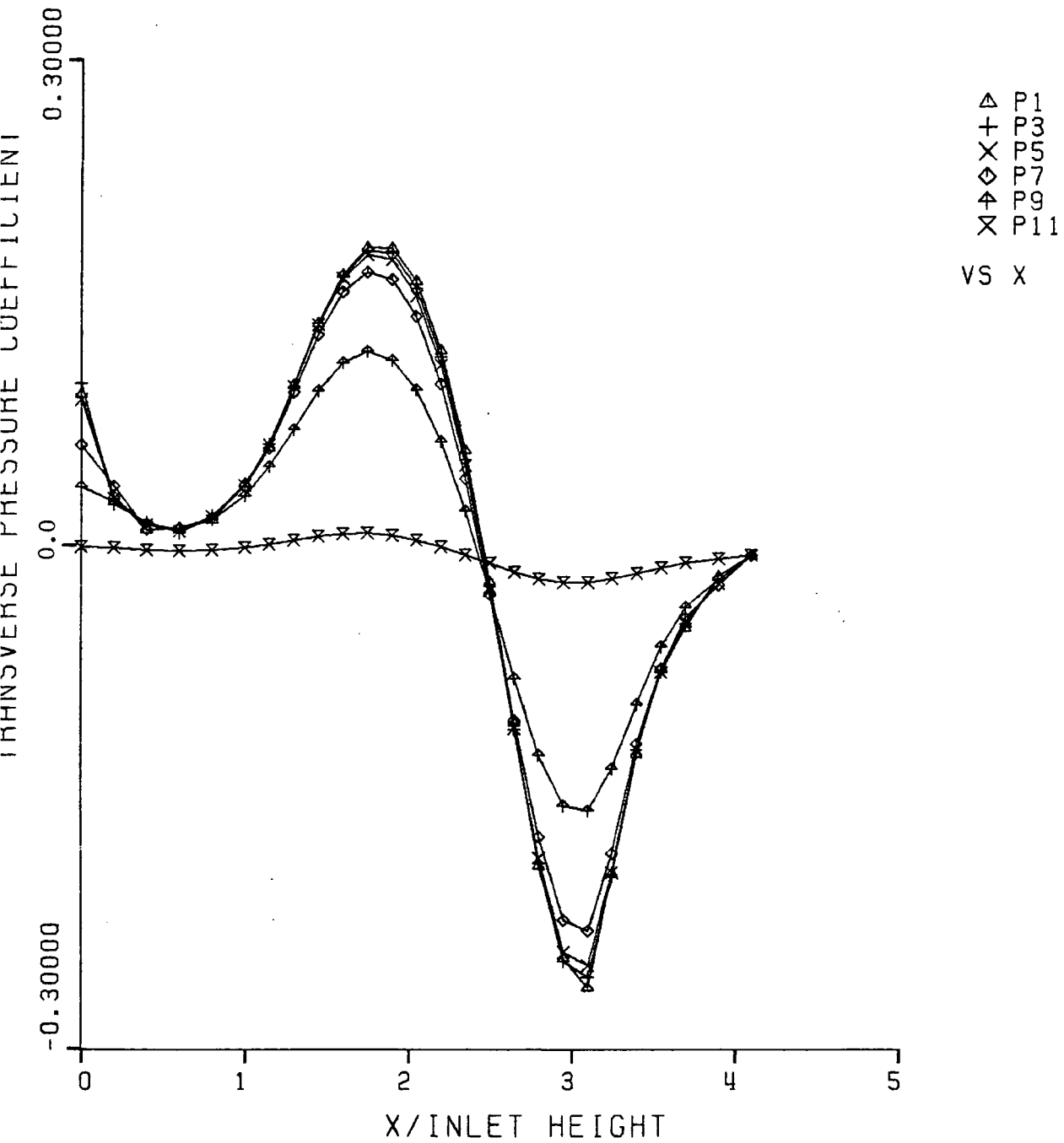


FIG. 2.11 TRANSVERSE PRESSURE COEFFICIENT  
NON-UNIFORM GRID  
INLET V-VELOCITY SPECIFIED

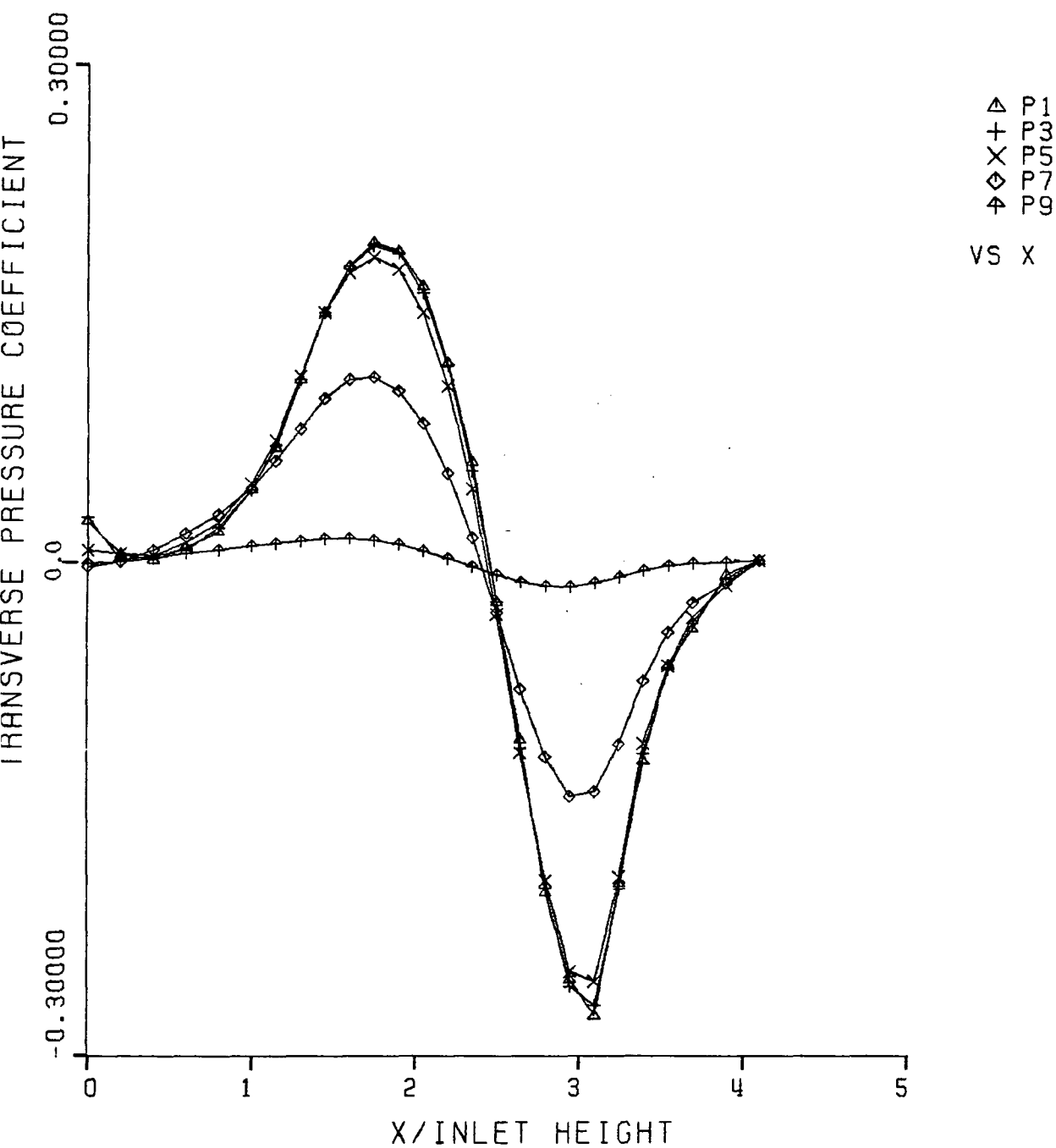


FIG. 2.12 PRESSURE COEFFICIENT  
NON-SMOOTH GEOMETRY NON-UNIFORM GRID

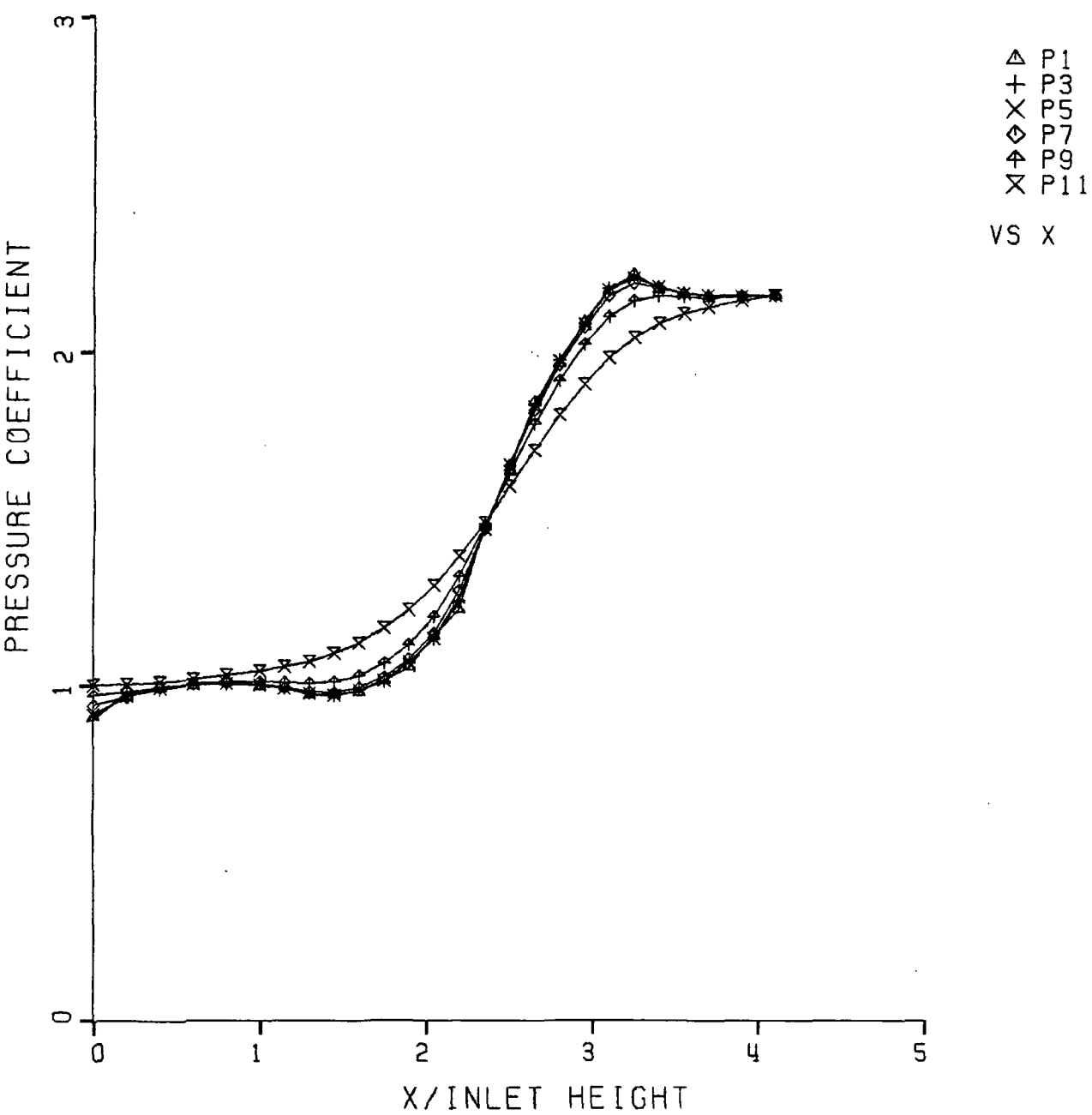


FIG. 2.13 PRESSURE COEFFICIENT  
SMOOTH GEOMETRY NON-UNIFORM GRID

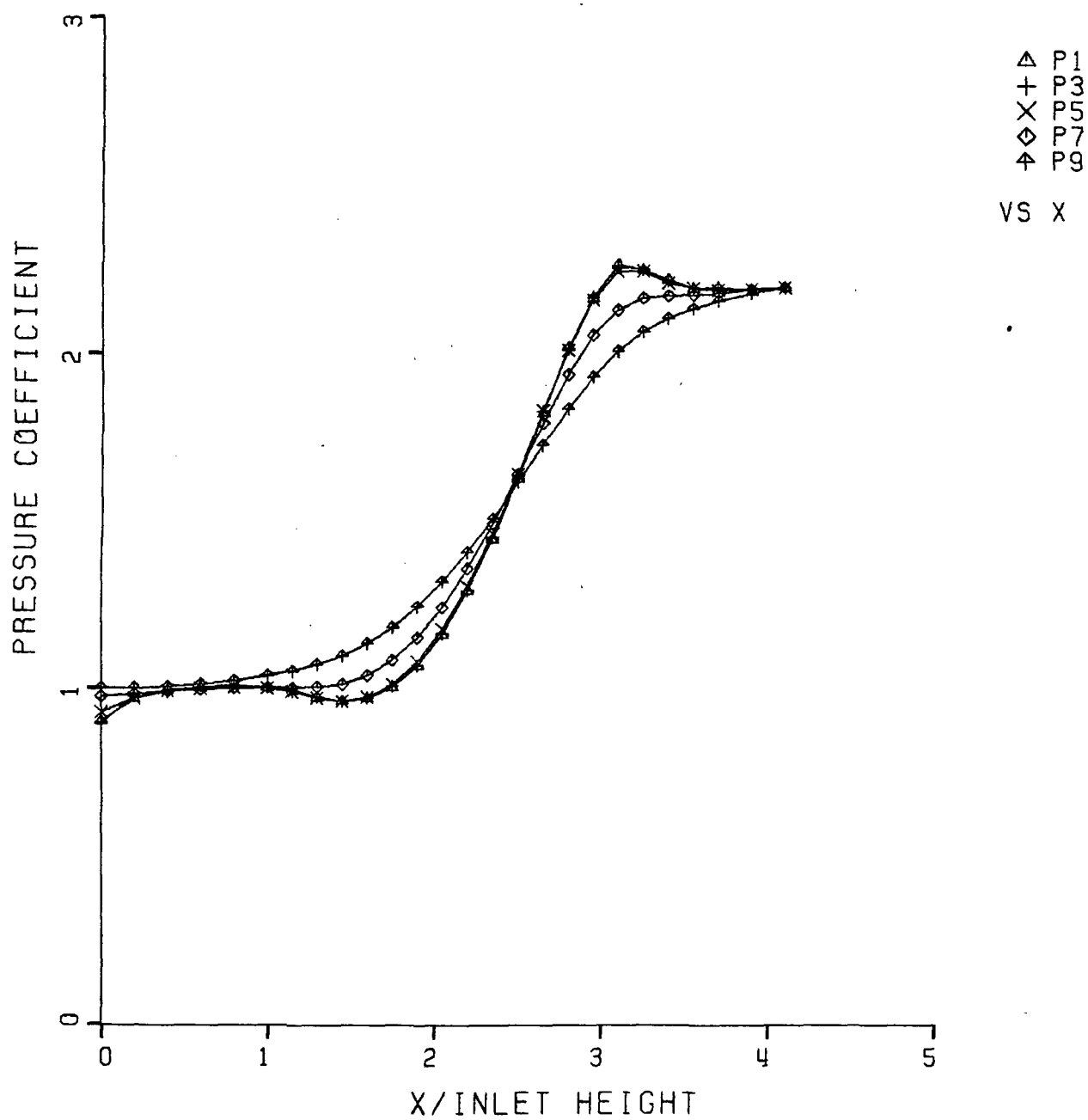




FIG. 2.14 PRESSURE COEFFICIENT  
SMOOTH GEOMETRY UNIFORM GRID

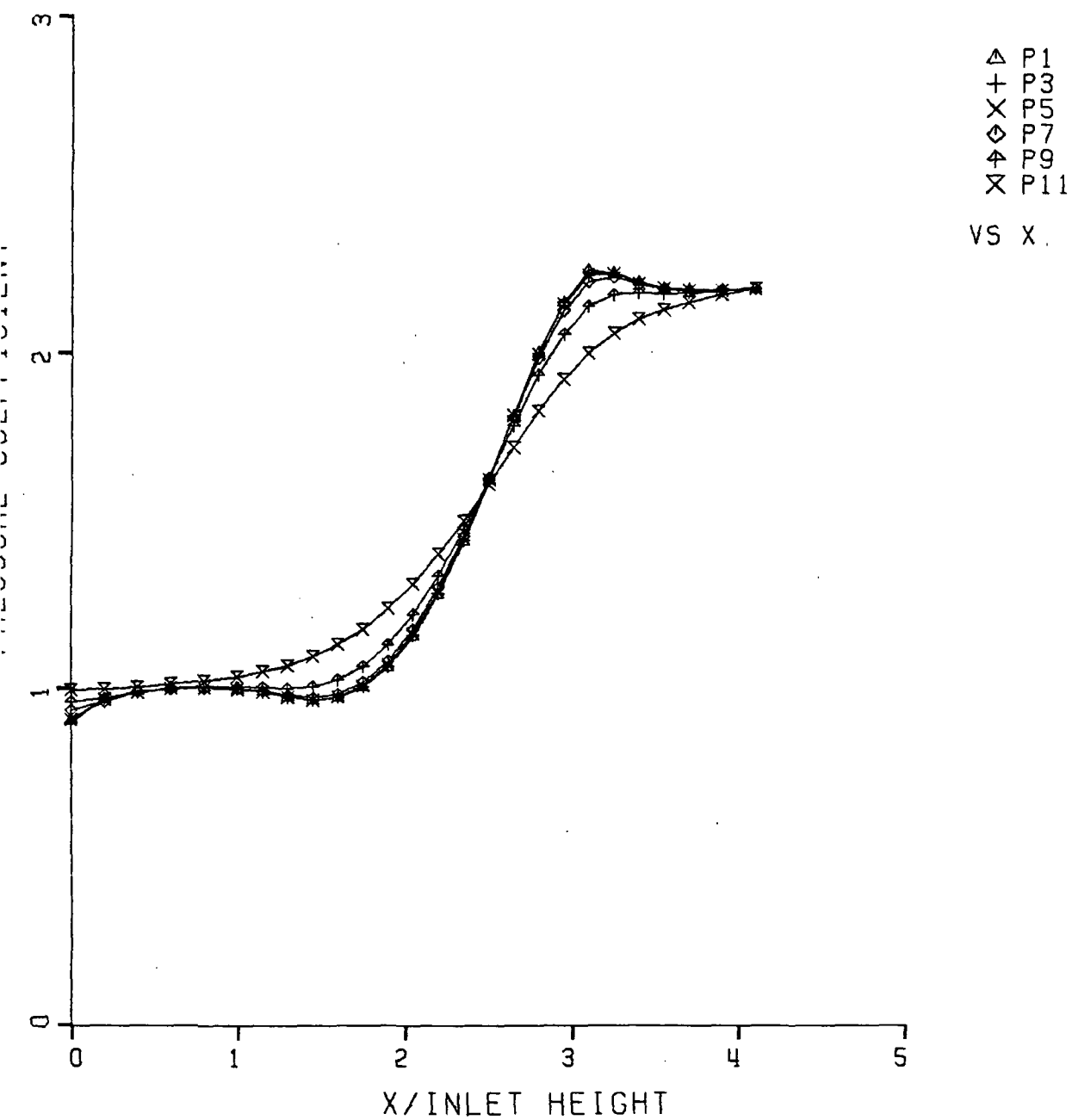
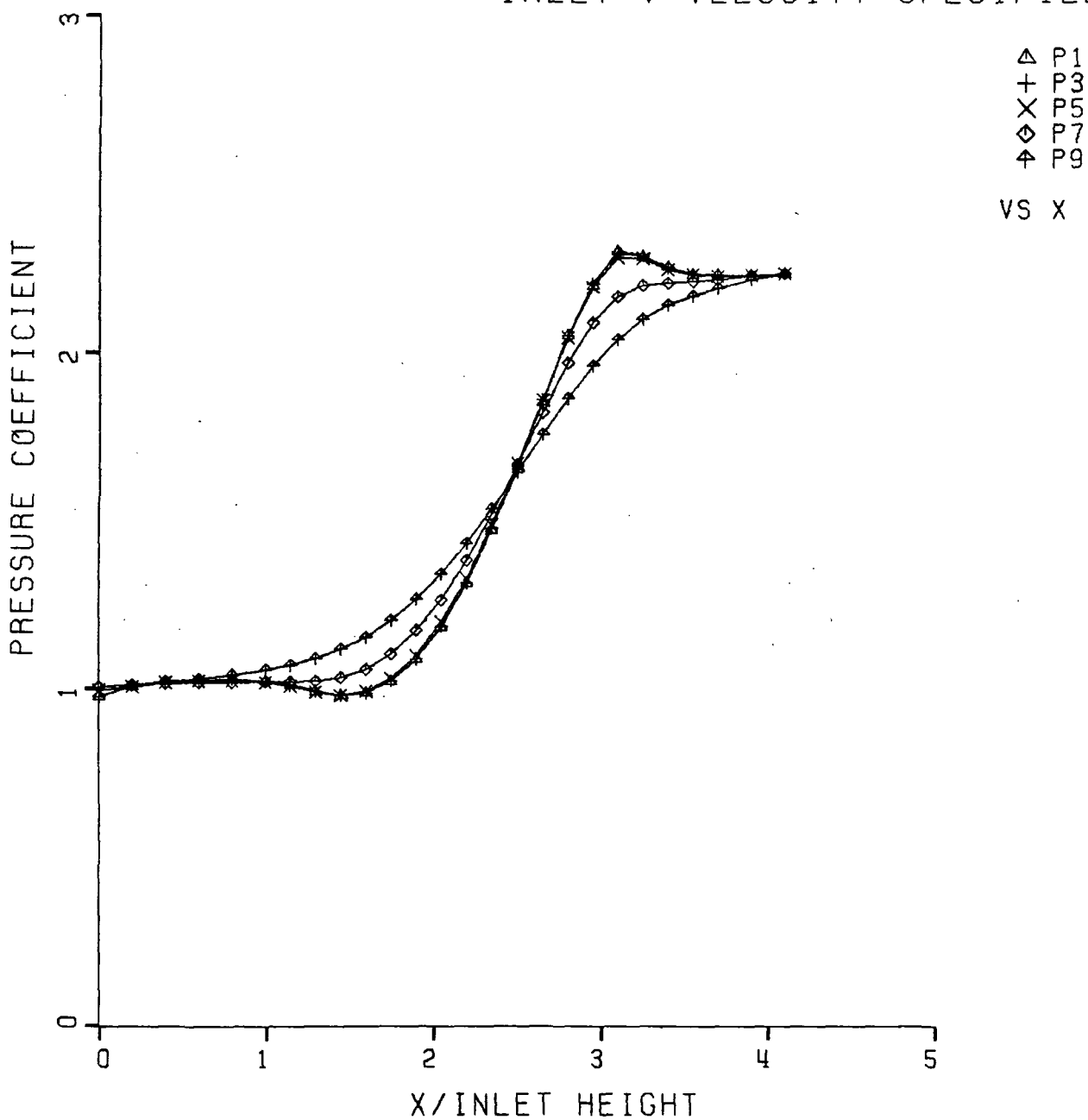


FIG. 2.15 PRESSURE COEFFICIENT  
NON-UNIFORM GRID  
INLET V VELOCITY SPECIFIED



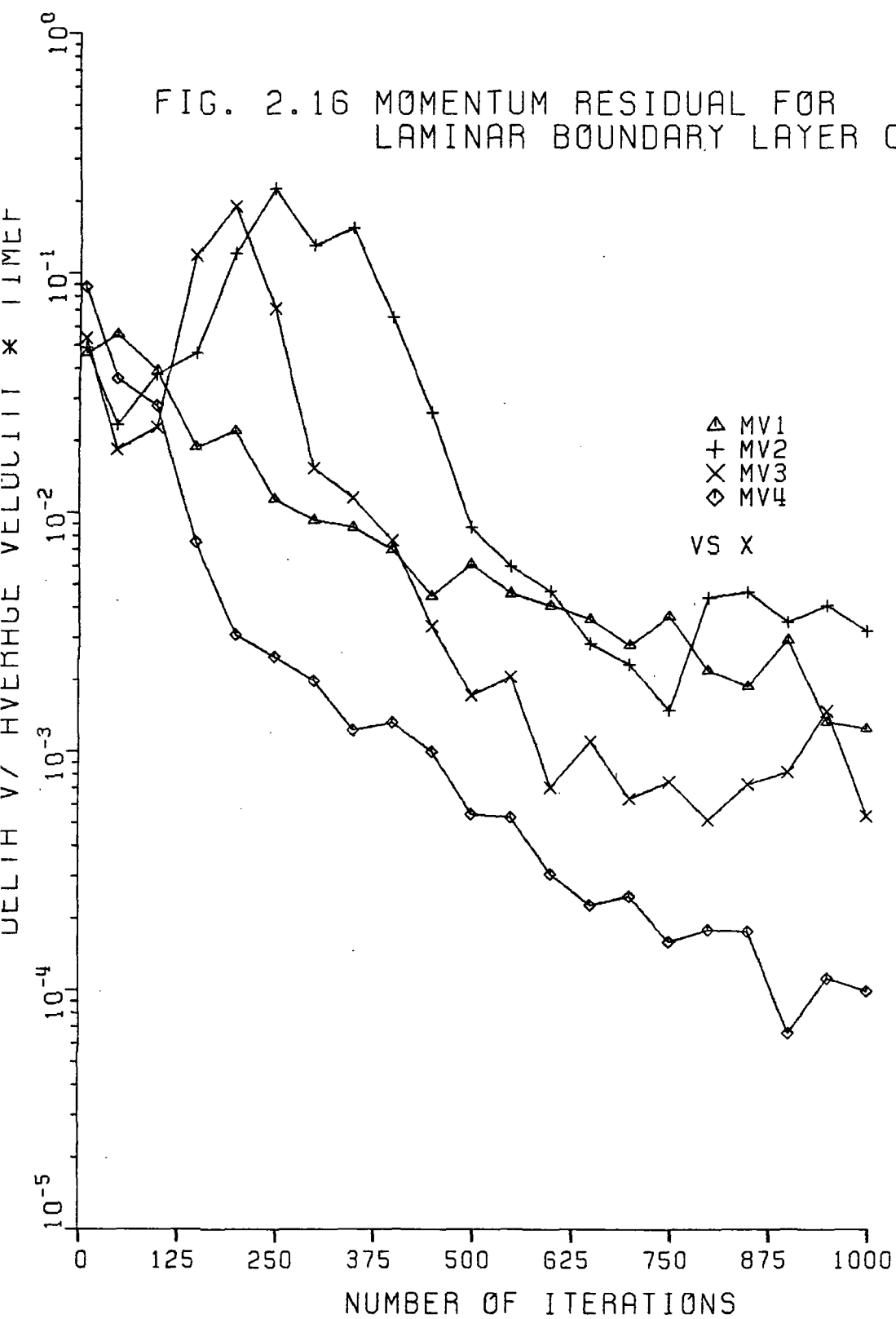
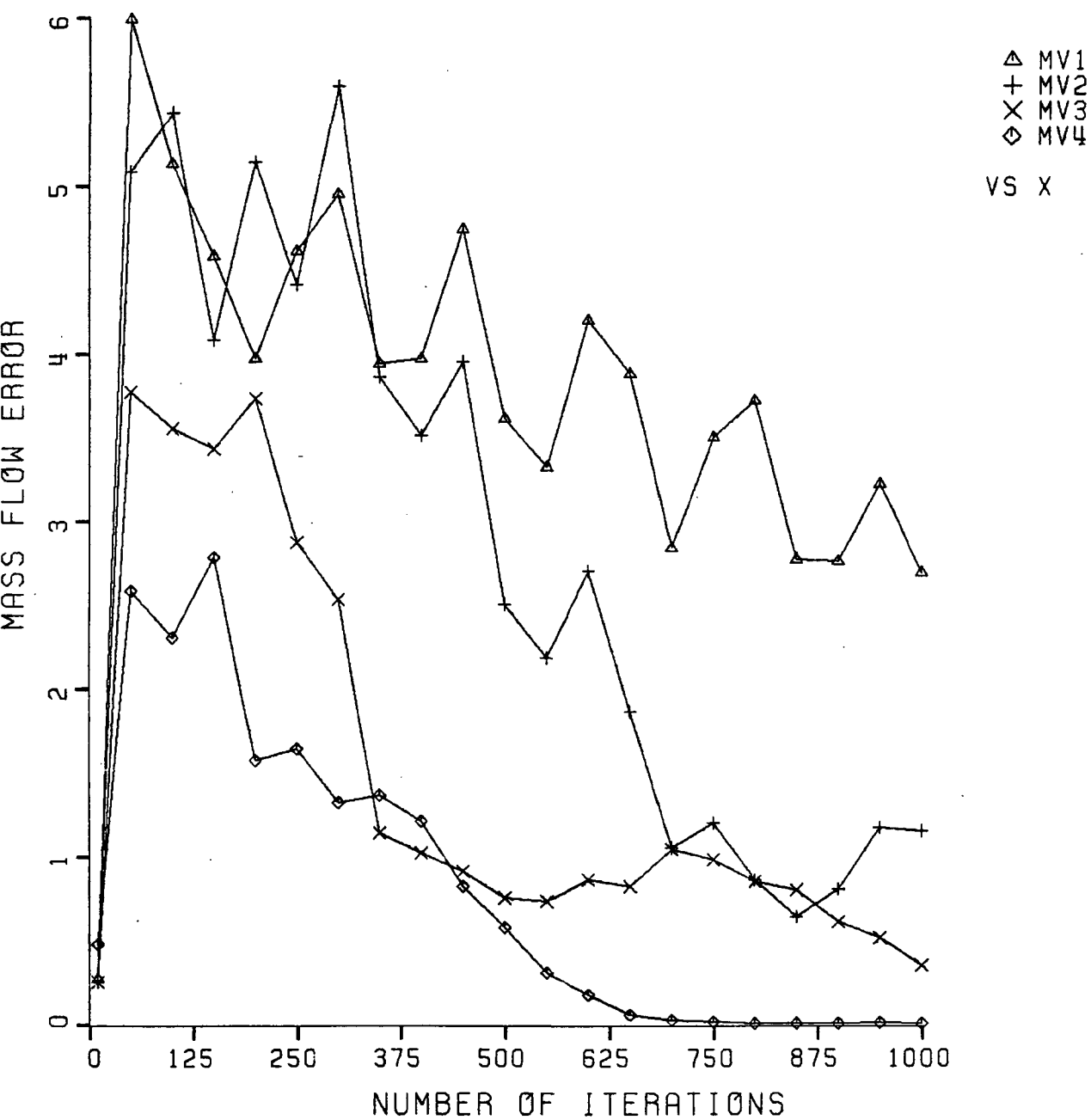


FIG. 2.17 MASS FLOW ERROR FOR  
LAMINAR BOUNDARY LAYER CALCULATION



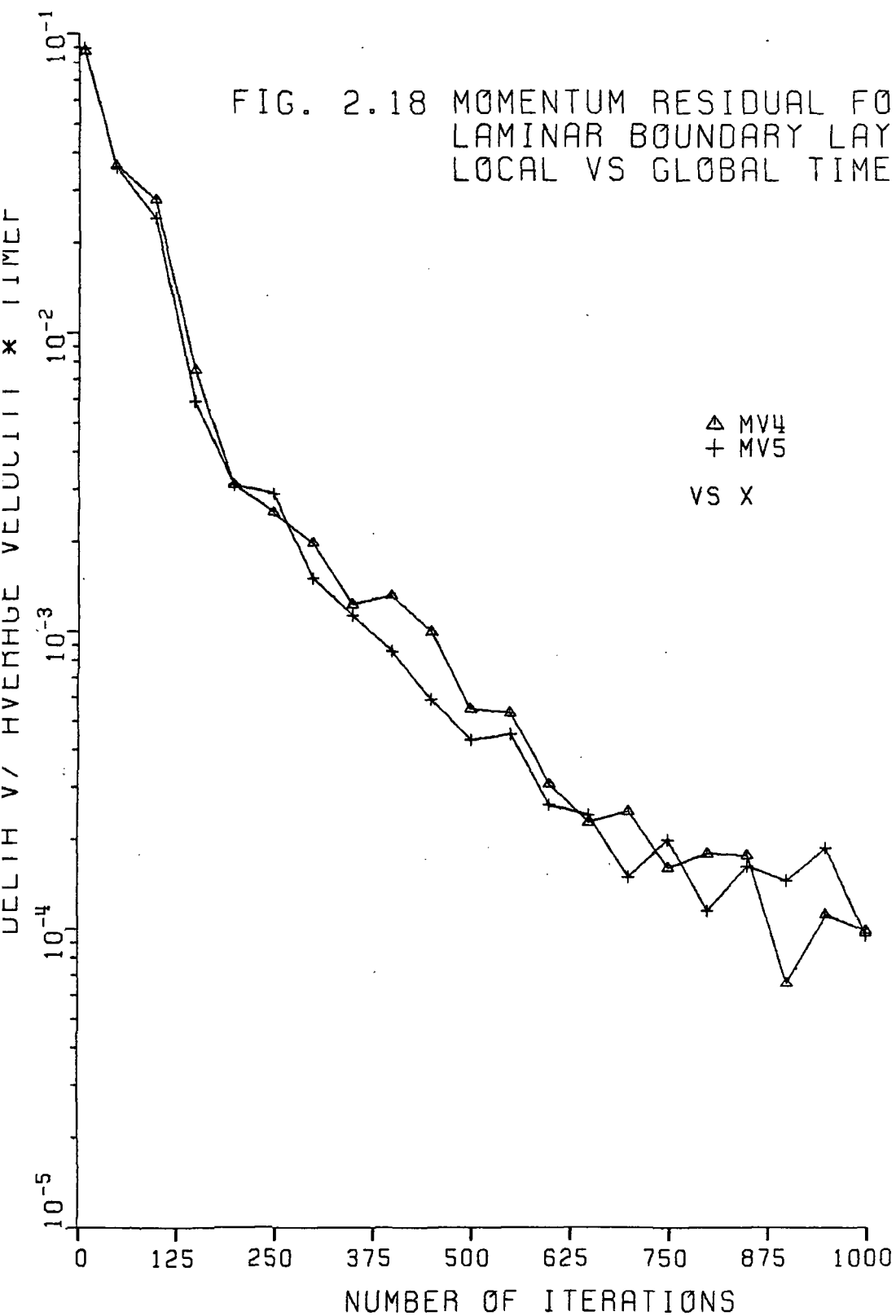
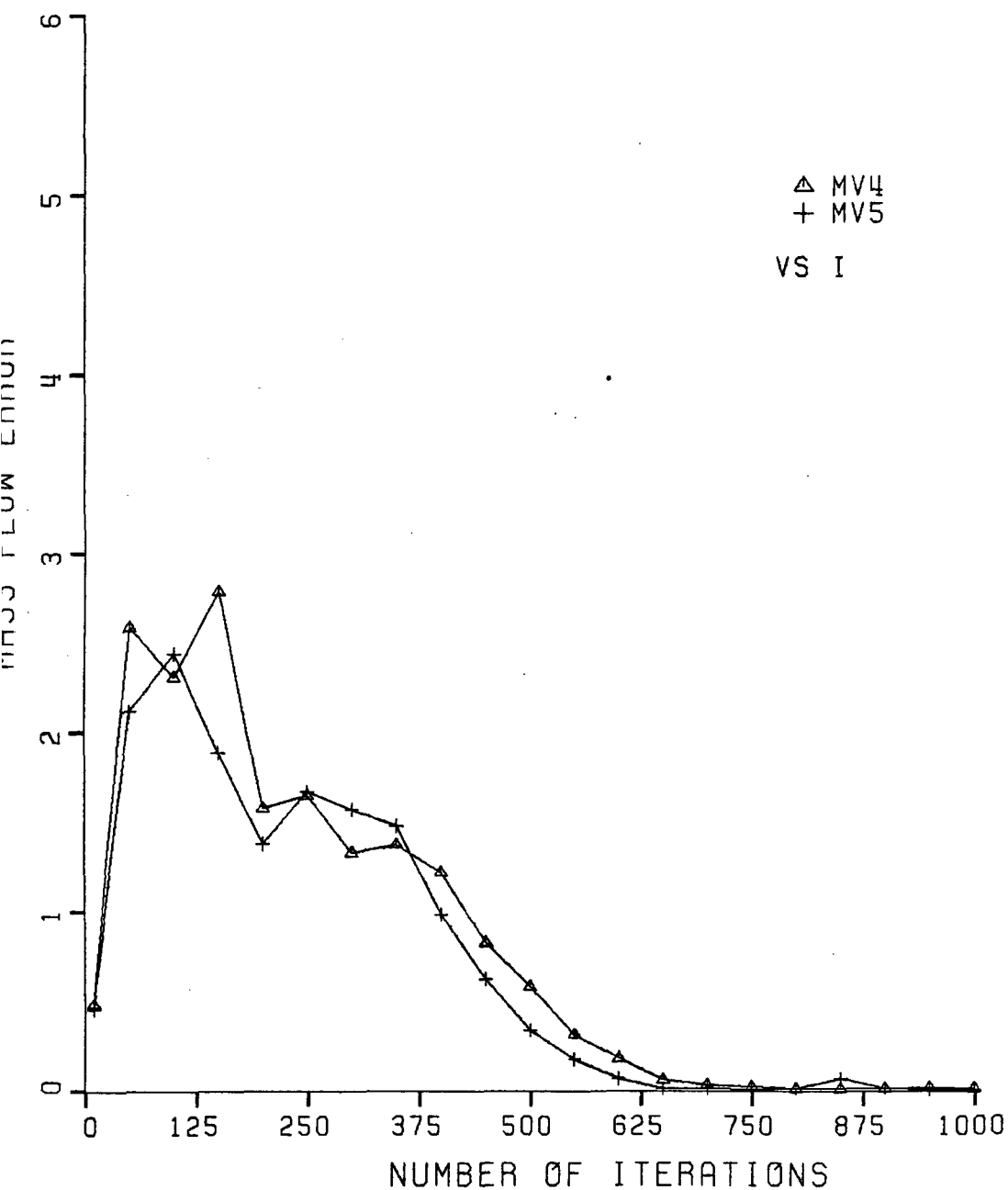


FIG. 2.19 MASS FLOW ERROR  
LAMINAR BOUNDARY LAYER CALCULATION  
LOCAL VS GLOBAL TIME STEPS



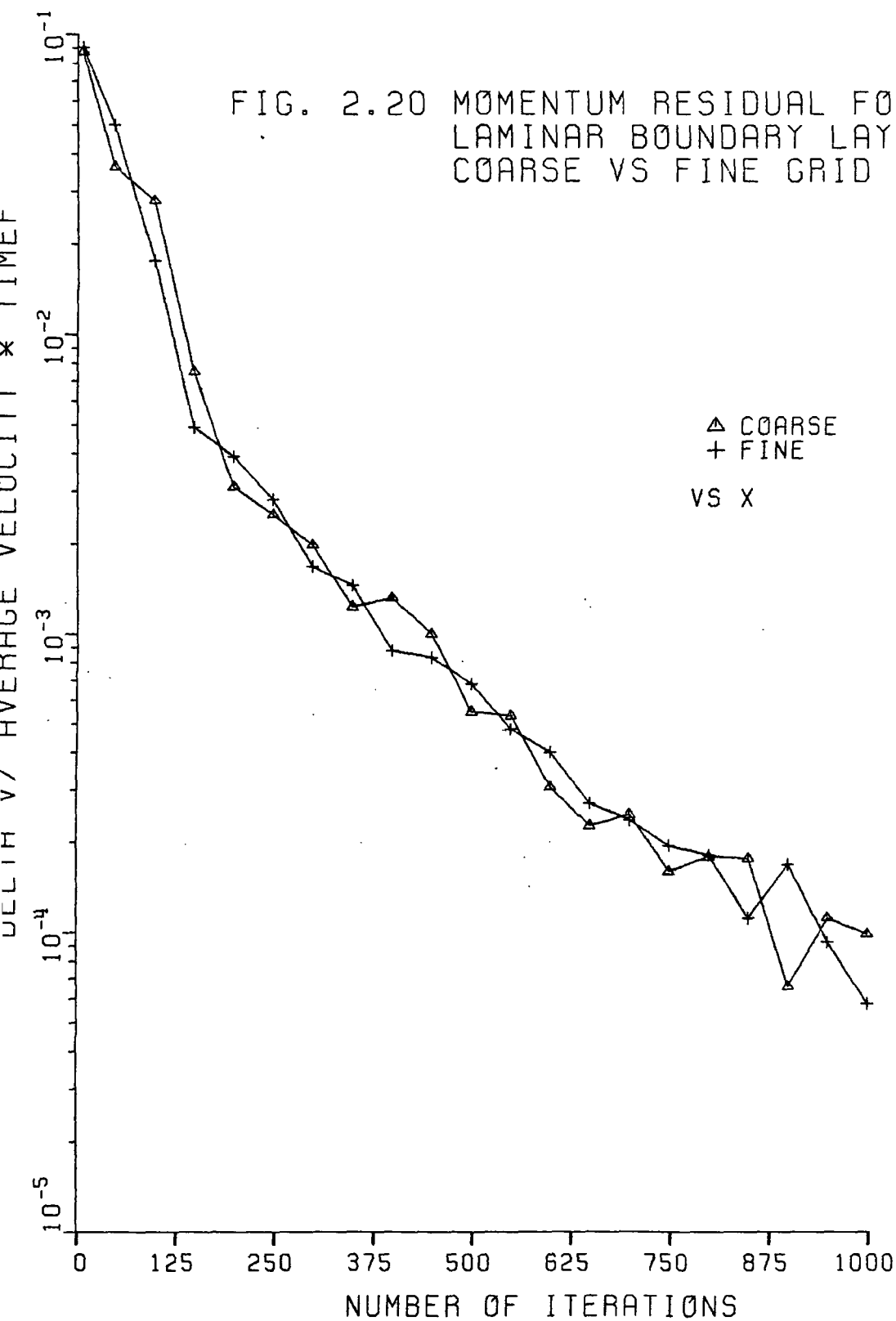
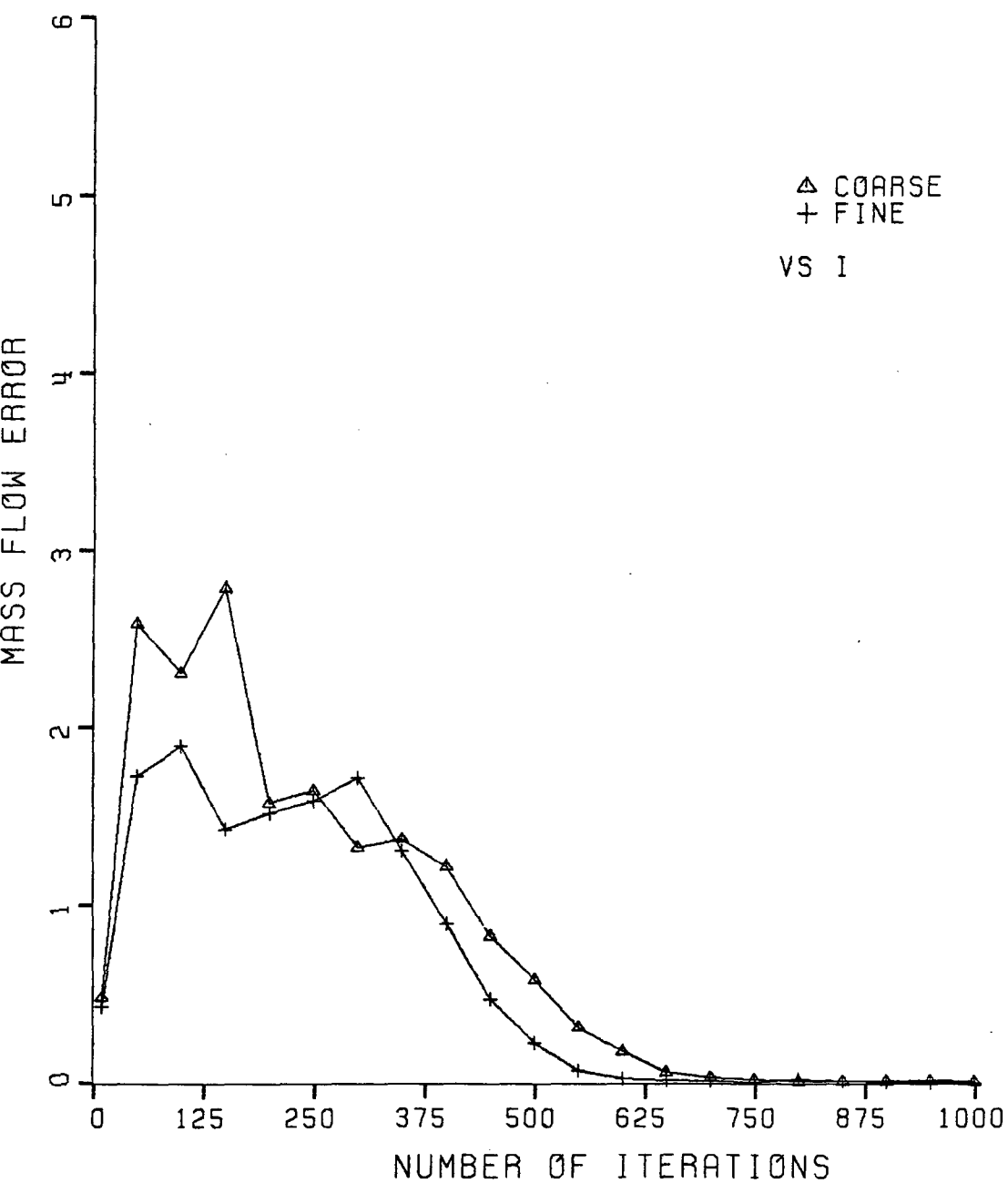


FIG. 2.21 MASS FLOW ERROR  
LAMINAR BOUNDARY LAYER CALCULATION  
COARSE VS FINE GRID





## SECTION 3 SAJBEN'S DIFFUSER CALCULATIONS

Additional calculations have been made for Sajben's transonic diffuser [ 6,7 ]. Previous calculations using this geometry were presented in Refs. 1 and 2. These were preliminary calculations to show that the method could be used to calculate viscous transonic flow. Refinements and corrections have been made to the code since those progress reports and the following results reflect those revisions and improvements. The improvements made to the method can be summarized as follows,

1. a new pressure interpolation scheme ( M&M formula ) is used to calculate the effective density ( Ref. 3 ).
2. a more complete treatment of the viscous stresses is included.
3. the amount of upwinding used in the transverse direction ( transverse upwind differencing ) is based upon a new criteria which is a function of the ratio of mass fluxes through the transverse and streamwise faces of a control volume.
4. an improved specification of the exit static pressure is used which reflects the side wall boundary layer blockage.
5. the boundary layers are calculated on both walls of the diffuser.

The diffuser geometry ( Model G ) is shown in Fig. 3.1; the throat height ,h, was 44 mm and the ratio of the exit height to throat height was 1.513. The calculations begin at  $x/h = -3.6$  and end at  $x/h = 8.2$ . Fig. 3.1 also shows the computational grid used which had 87 grid points in the axial direction and 20 points across the flow. The radial distribution of grid points used is shown in Table 3.1. The development of a turbulent boundary layer was modeled on both the curved and the flat walls. The inlet boundary layer thicknesses were specified as 9 % and 4.5 % of the inlet diffuser height for the curved and flat wall boundary layers, respectively. An absolute viscosity of

Table 3.1 Radial Distribution of Grid Points

1	0.0005
2	0.0020
3	0.0050
4	0.0110
5	0.0230
6	0.0470
7	0.0950
8	0.1910
9	0.3080
10	0.4305
11	0.5695
12	0.6920
13	0.8090
14	0.9050
15	0.9530
16	0.9770
17	0.9890
18	0.9950
19	0.9980
20	0.9995

0.000018 kg/ m s was used. The inlet total pressure was 135 kPa and the inlet total temperature was 300 K.

For this calculation, the ratio of the exit static pressure to the inlet total pressure was 0.826. This computational exit static pressure is equal to the experimental exit static pressure plus a correction in pressure for the side wall boundary layer blockage. Suction slots upstream of the throat and downstream of the exit plane reduce the side wall boundary layer blockage and improve the two-dimensionality of the flow. However, the side wall boundary layers do affect the effective flow area of the diffuser and the two dimensional computations must reflect this when a suitable exit static pressure is chosen. Therefore the exit static pressure of 0.826 is 1.5 % greater than the experimental static pressure because of the blockage effect of the side wall boundary layers. In the experiment, this test point results in transonic flow in the diverging portion of the duct with a Mach number of approximately 1.235 upstream of a nearly normal shock, and the flow remained fully-attached throughout the diffuser at this test condition.

A plot of static pressure contours is shown in Fig. 3.2. The shock can be seen in the diverging portion of the duct. The shock is well defined as illustrated by the high clustering of contours at the shock. The M&M formula (3) is used to calculate the the interpolated pressure which is used in the calculation of the effective density. Fig. 3.3 shows a Mach number contour plot for the calculations. The extent of the boundary layer can be seen from this figure.

The calculated and measured curved wall static pressures are compared in Fig. 3.4. The shock is very well defined and no overshoot occurs in the static pressure. The static pressures do not agree so well downstream of the shock because the 2-D calculations do not reflect the rapid increase in the side wall boundary layer thickness and its effective blockage. The point of minimum static pressure in the calculations is located at  $x/h = 1.5$ . This is taken to be the location of shock. The Mach number upstream of the shock was determined to be 1.256 from the calculated total pressure ratio across the shock in the freestream.

The computed and measured shock locations on the curved wall are compared in Fig. 3.5. The variable  $x_{su}$  is the shock location on the curved wall and  $x_{sm}$  is the shock location in the middle of the duct. The Mach number upstream of the shock, determined from static pressure measurements, is represented by  $M_{su}$  in Fig. 3.5.

The Mach number distribution through the nozzle at a fixed  $y/h$  of 0.0905 is shown in Fig. 3.6. This grid line was chosen because the maximum Mach number is located along it. The shock is sharp and no overshoots or undershoots occur.

Comparisons of calculated and measured velocity profiles ( see Ref. 7) at four axial locations along the duct are shown in Figs. 3.7, 3.8, 3.9, and 3.10. The axial locations are  $x/h = 2.31, 4.03, 6.34,$  and  $8.2$  respectively. The agreement is good especially at the two downstream stations. The velocities in Figs. 3.7-3.10 are normalized with respect to the maximum computed or measured velocity in the duct at that axial location, which ever is applicable. In the calculations, the edge of the boundary layer is located where the normalized total pressure gradient is 25.0. It may be noted that the present calculations give much better agreement with the measured velocity profiles than the calculations of Liou, Coakley, and Bergmann of Reference 8 ( see Fig. 3.17). Other investigators who have used Sajben's diffuser as a test case have not shown a comparison of their computed velocity profiles with the measurements of Ref. 7.

Fig. 3.11 shows static pressure contours for calculations which were made using the three-point scheme for the interpolated pressure. The shock resolution is not nearly as well defined as that obtained when the M&M formula is used. Fig. 3.12 shows the corresponding Mach number contour plot when the three point interpolation scheme is used.

The distribution of loss generation in the diffuser will be presented in three ways. First, the losses due to curved wall boundary layer, the flat wall boundary layer, and the shock loss in the freestream are compared in Fig. 3.13. These losses were determined by first calculating the mass flow rates in the boundary layers and the freestream at the diffuser exit using the calculated boundary layer

Table 3.2 Example Calculation of Total Pressure  
Loss for a Boundary Layer

$$\bar{P}_{t\text{-losses}} = \frac{\int_0^{\dot{m}_s} (P_{t\text{-inlet}} - P_{t\text{-local}}) \cdot d\dot{m}}{\dot{m}_{\text{total}}}$$

\* where  $\dot{m}_{\text{total}}$  is the total mass flow rate through a given cross-section of the diffuser, and  $\dot{m}_s$  is the mass flow rate in the boundary layer at the exit.

thicknesses as the boundaries between regions. Then the mass averaged total pressure loss at each axial location was calculated by integrating the total pressure loss out to these fixed mass flow rate values and then normalizing these losses with respect to the inlet freestream total pressure ( see Table 3.2). All three losses are approximately the same. The curved wall ( bottom wall ) boundary layer contributes the largest proportion to the total losses because the boundary layer is thicker there.

The total pressure loss along an inviscid streamline is compared with the mass averaged total pressure loss for the entire cross-section of the diffuser in Fig. 3.14. This figure allows another means of comparing the shock and total losses. The total pressure loss through the shock is very well defined. The mass averaged total pressure loss through the shock is approximately 30% greater than the shock loss alone.

The mass averaged total pressure divided by the inlet freestream total pressure at the diffuser exit is calculated from the numerical results to be 0.9615. From data given to us by M. Sajben and T. Bogar, the mass averaged total pressure calculated from the experimentally measured data is 0.965. The experimental data used for this calculation was measured midway between the side walls. The agreement is good.

The measured maximum Mach number in the exit plane of 0.51 agrees well with the calculated value of .511. The boundary layer thicknesses are measured to be approximately 25% of the duct height on the curved wall and 23 % of the duct height on the flat wall. The calculations determined the boundary layer thickness on the curved wall to be 25% of the duct height and 23% of the duct height of the flat wall.

The above calculations are after 5000 iterations using a TIMEF of 4.0. It may have been possible to run the calculation with a TIMEF of 2.0 after the initial transients but because of computer cost this option was not attempted for this test case. The momentum residual for this calculation is presented in Fig. 3.15. The continuity error after 5000 iterations was less than .1%. The unusual

behavior observed between 3000-4000 iterations in Fig. 3.15 appears to be typical of the method in general when transonic flow is calculated. The same general convergence behavior is seen for the 1-D nozzle ( Ref. 3 ) in Fig. 3.16. A time factor of 2.0 was used for these 1-D calculations but the same behavior is seen here on a smaller time scale. The total CPU time for the Sajben calculations was approximately 35 minutes on the IBM 3031.

A number of other workers have used this test case to verify the accuracy of their computational methods ( 8, 9, and 10 ). Liou, Coakley, and Bergmann's (8) calculations were made using a MacCormack type scheme in conjunction with a two-equation model for the turbulent stress predictions. For the weak shock case, they used an exit static pressure of  $0.8 \times P_{t,inlet}$ . There was good agreement between their computed and measured wall static pressures. However, the calculated velocity profiles were not in good agreement with the experimental data. Fig. 3.17 shows a sample of their results.

Liu, Shamroth, and McDonald (9) used this test case to verify their computational method which solves the governing equations using a consistently split linearized block implicit scheme. A mixing length model was used to model turbulent stresses. For the weak shock case, an exit static pressure of  $0.807 \times P_{t,inlet}$  was used. They compared their computed wall static pressures with the experimental pressures and found good agreement (see Fig. 3.18). The variable  $\sigma$ , referred to in Fig. 3.18 is the value of the artificial dissipation parameter used in their calculations. They found that for values of  $\sigma$  less than 0.1 the solution was invariant. Also presented in Ref. 9 were static pressure and Mach number contour plots for this weak shock case. These contour plots are similar to those in Figs. 3.2 and 3.3. The shock definition in the present work is sharper than Liu et. al. but fewer axial grid points were used in their calculations. No comparison was made by Liu, Shamroth, and McDonald between the measured and computed velocity profiles.

Talcott and Kumar (10) also used the weak shock case for Sajben's diffuser as a test of their computer program's accuracy. They used an implicit MacCormack scheme to solve the governing equations and a Baldwin-Lomax mixing length turbulence model to predict the turbulent stresses.

They also used an exit static pressure of  $0.807 \times P_{t, inlet}$ . Fig. 3.19 shows a sample of their results. They present a static pressure contour plot for this weak shock case. As with Liu et. al., the shock definition of Talcott and Kumar's method is not as sharp as that obtained using the present method but again they have used fewer axial grid points in their calculations. Also, the static pressure contours at the throat of the diffuser are erratic. A plot of wall static pressure is also presented. No comparison was made between the computed and measured velocity profiles.

In summary, the following observations can be made about the present calculations of the weak shock case in Sajben's diffuser.

1. There is better agreement between measured and calculated velocity profiles when the present method and static pressure specification are used.
2. The present method compares favorably with other methods in the areas of static pressure and Mach number contour predictions and wall static pressure prediction.
3. The agreement between calculated and measured mass averaged total pressure losses for the diffuser is excellent.



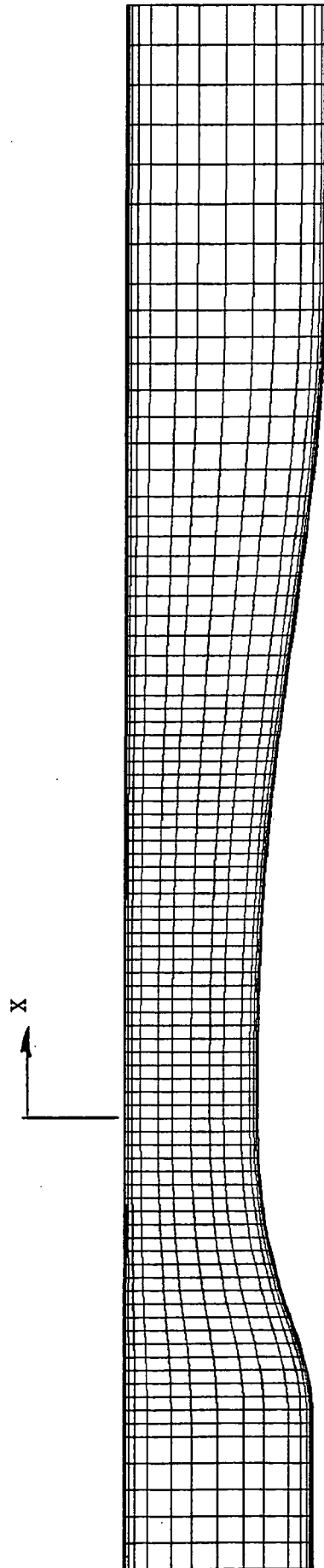


Fig. 3.1 Geometry and Grid for Sajben's Diffuser Calculations

5000 ITERATIONS PB=111.5 KPA  
P AT C=1.00

3.10

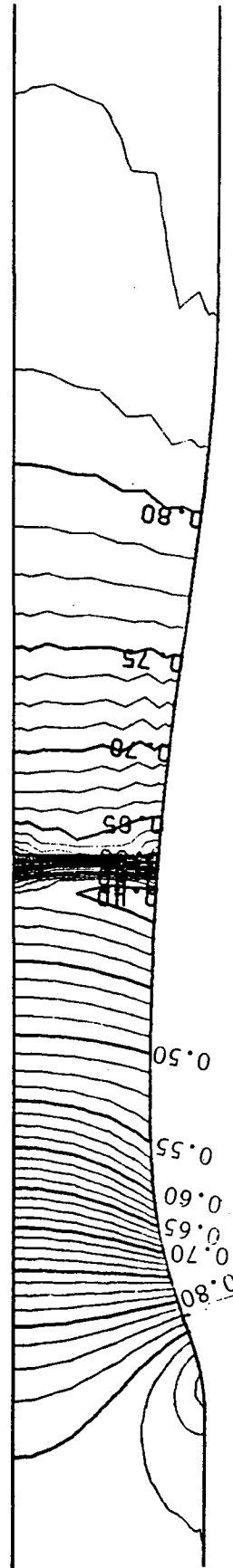


Fig. 3.2 Static Pressure Contours for Sajben's Diffuser  $P/P_{t,inlet}$

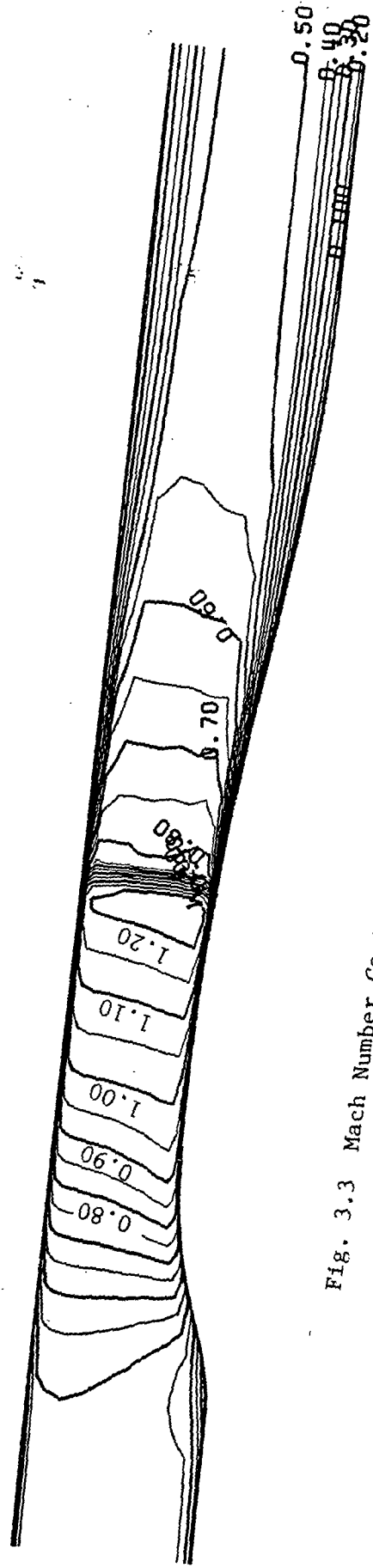
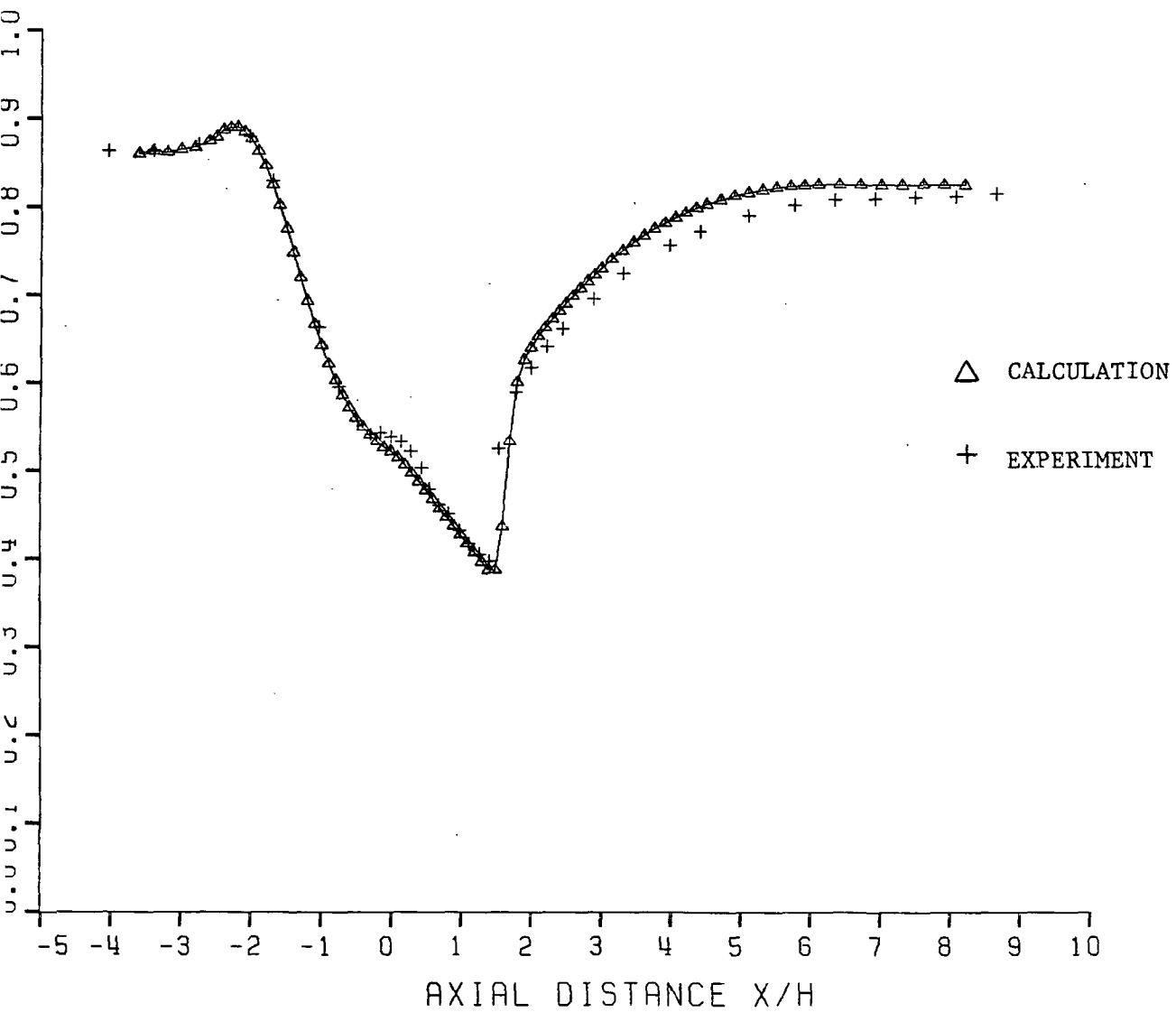


Fig. 3.3 Mach Number Contours for Sajben's Diffuser

5000 ITERATIONS  
MACH AT C = 1.00  
PB=111.5 KPA

ORIGINAL PAGE IS  
OF POOR QUALITY

FIG. 3.4- STATIC PRESSURE FOR 111.5 KPA  
5000 ITERATIONS  
CALCULATION VS EXPERIMENT



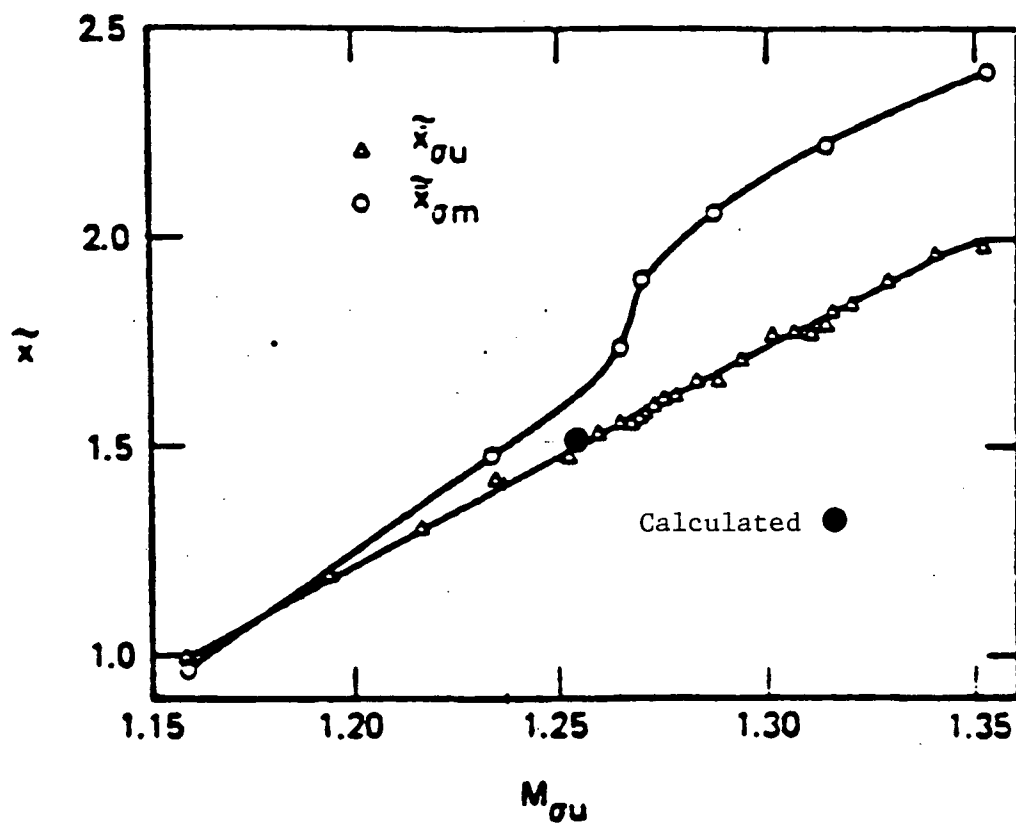


Fig.-3.5 Comparison of Computed and Measured Shock Position

FIG. 3.6 MACH NUMBER ALONG GRID LINE  
AT  $Y/H=0.0950$

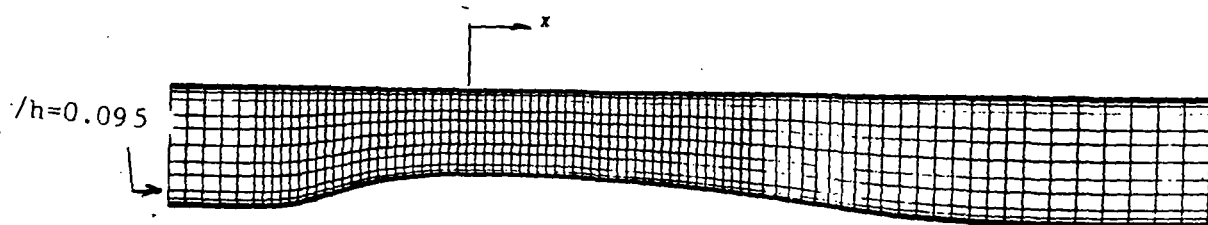
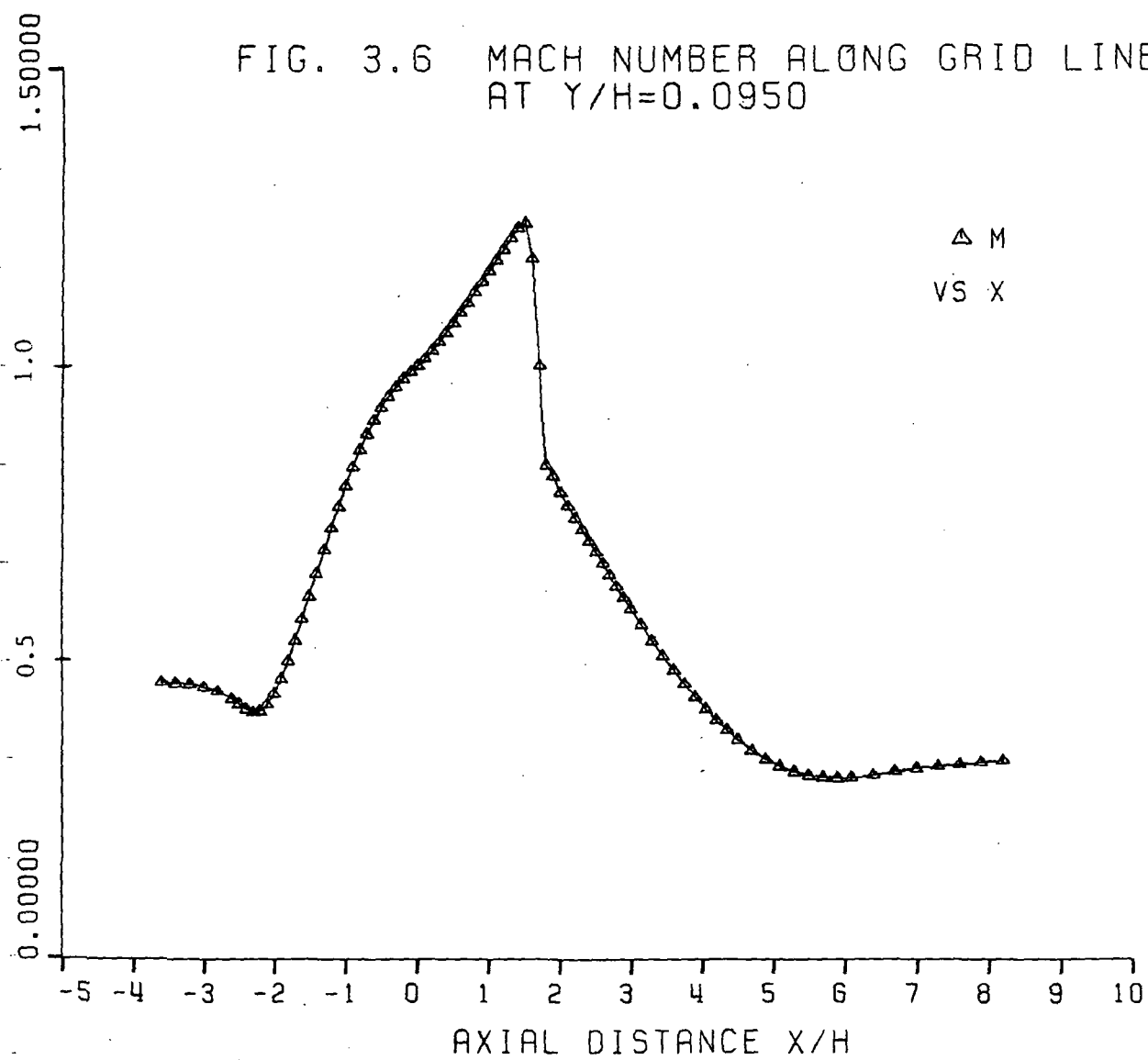


FIG. 3.7 VELOCITY PROFILE AT  $X/H=2.31$

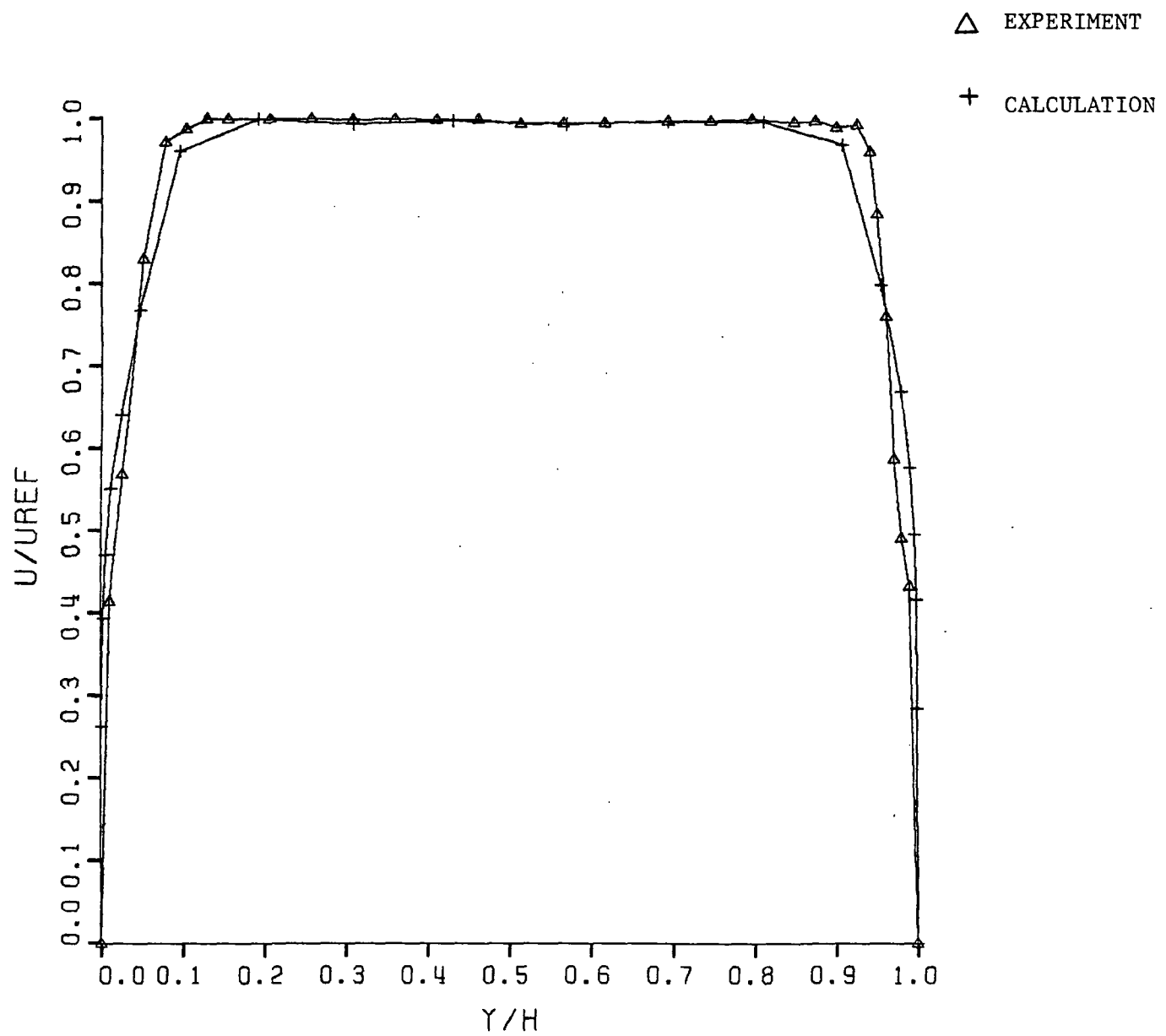


FIG. 3.8 VELOCITY PROFILE AT  $X/H=4.03$

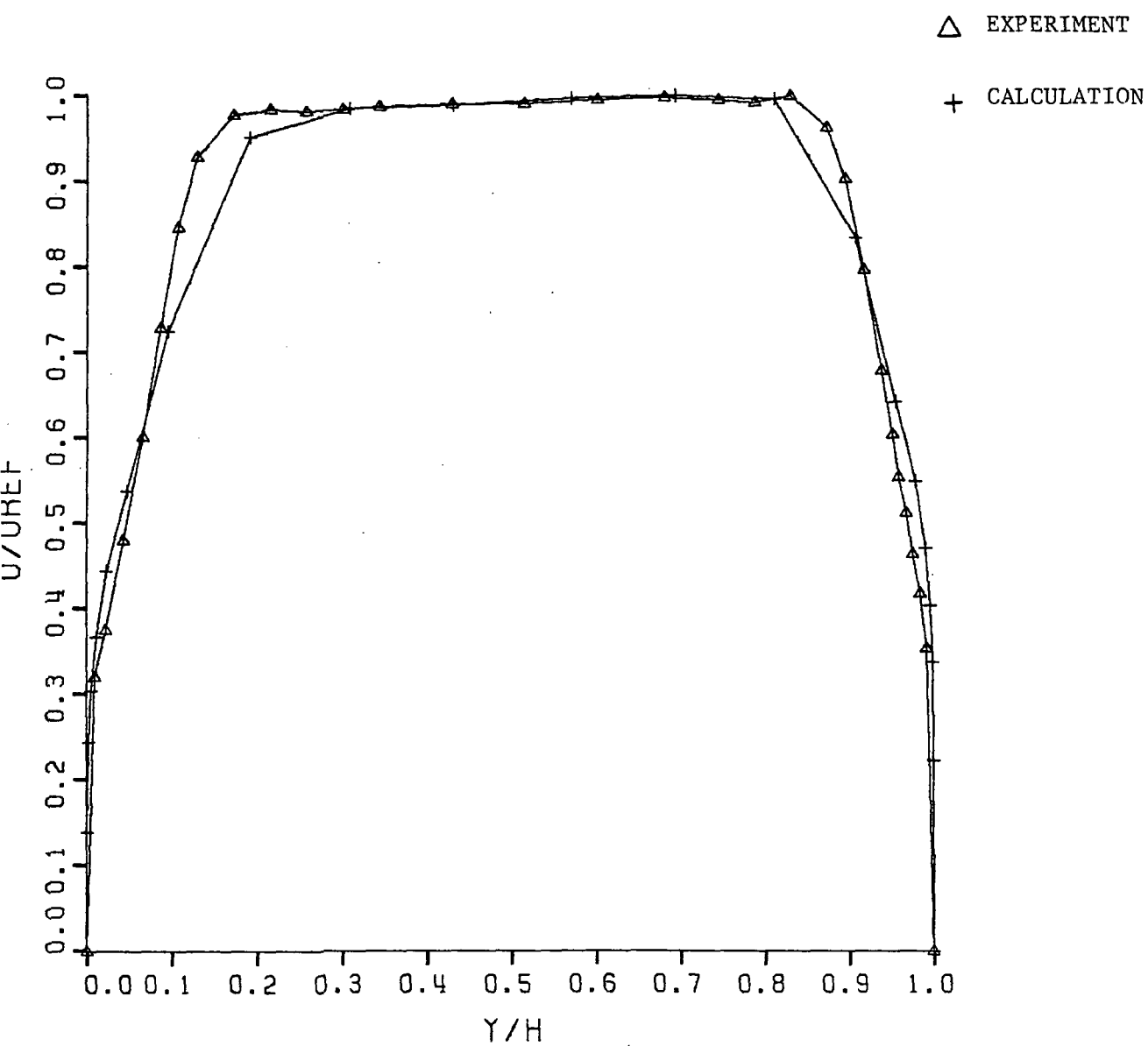




FIG. 3.9 VELOCITY PROFILE AT  $X/H=6.34$

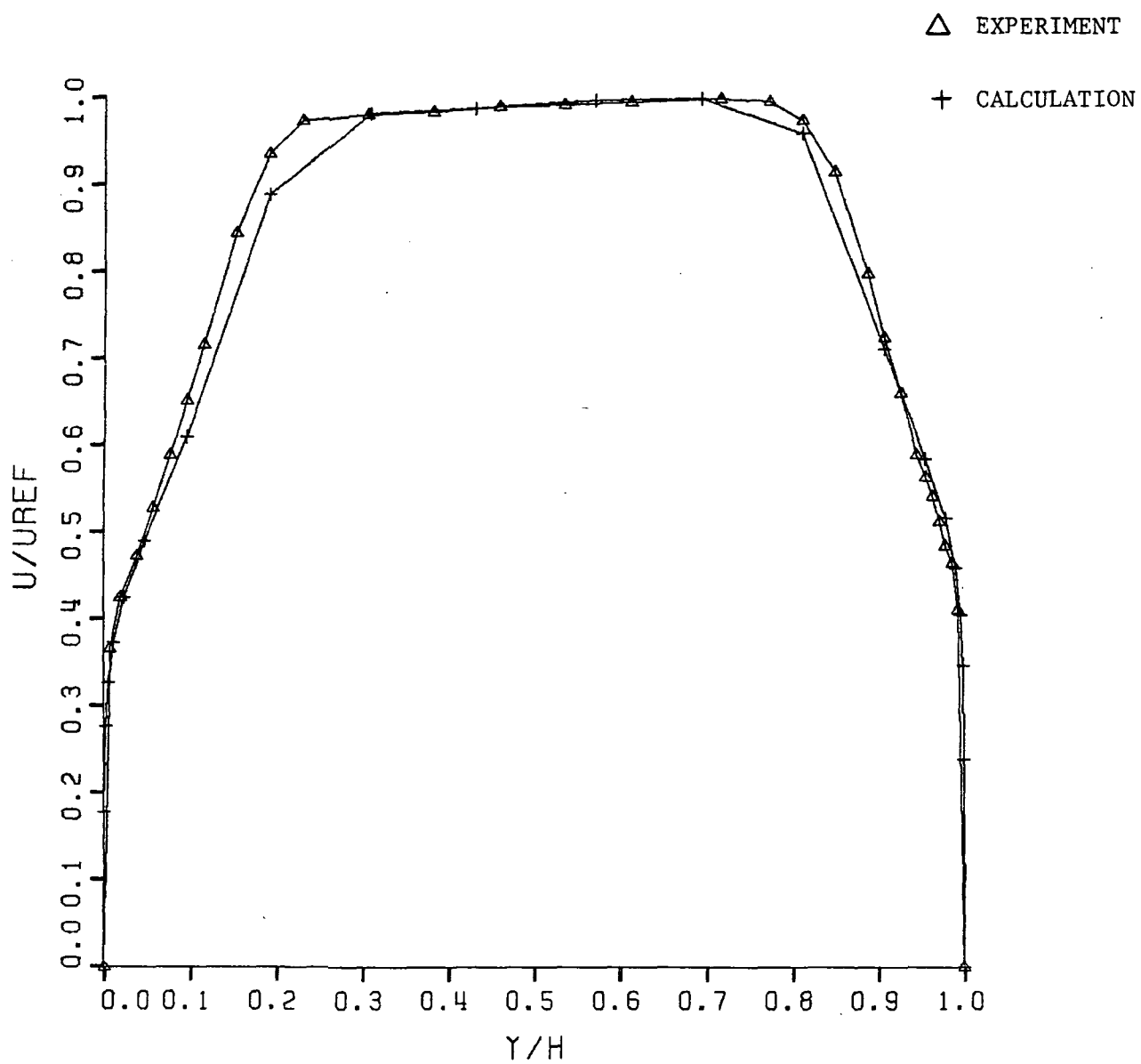
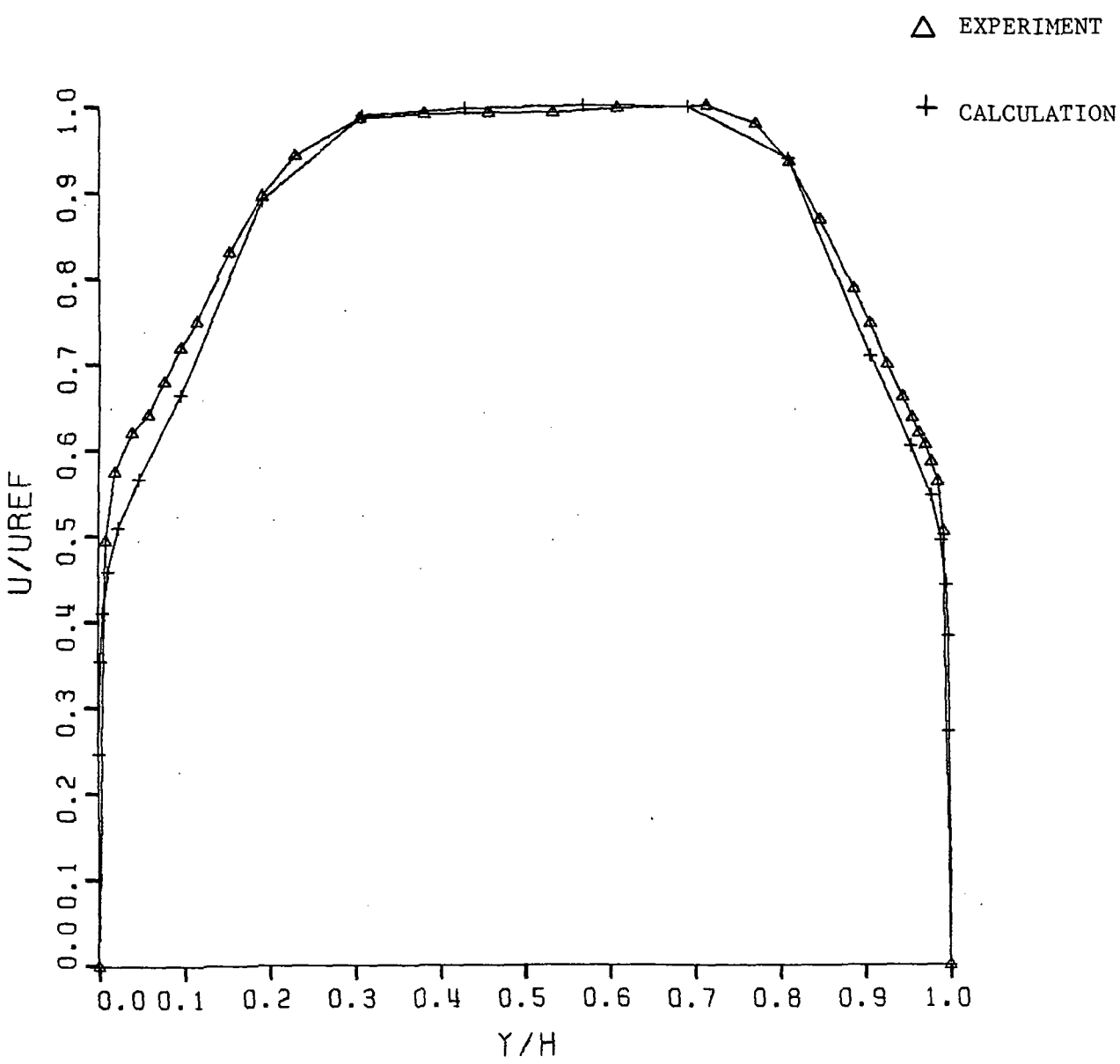


FIG. 3.10 VELOCITY PROFILE AT  $X/H=8.20$



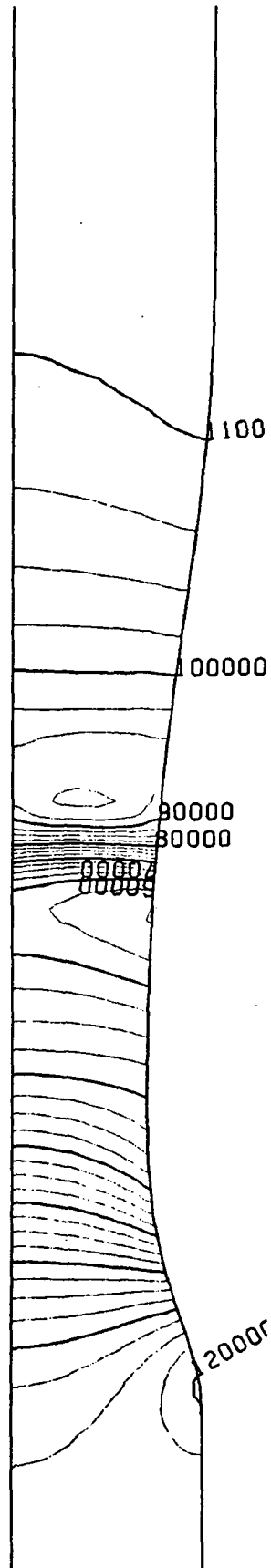


Fig. 3.11 Static Pressure Contours for Sajben's Diffuser  
Using Three Point Interpolation Scheme

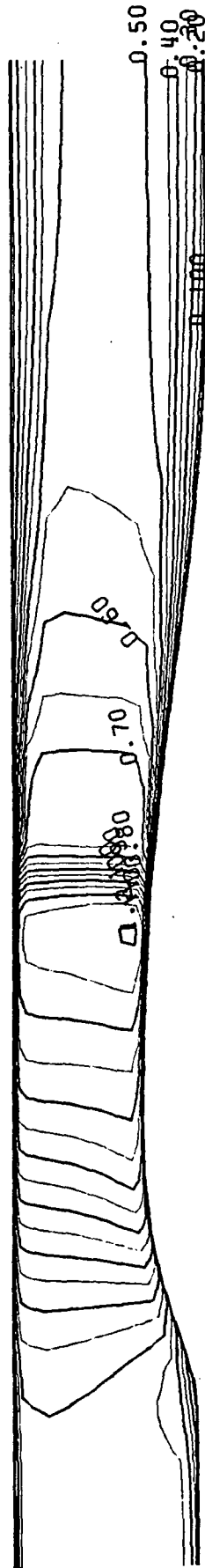


Fig. 3.12 Mach Number Contours for Sajben's Diffuser  
Using Three Point Interpolation Scheme

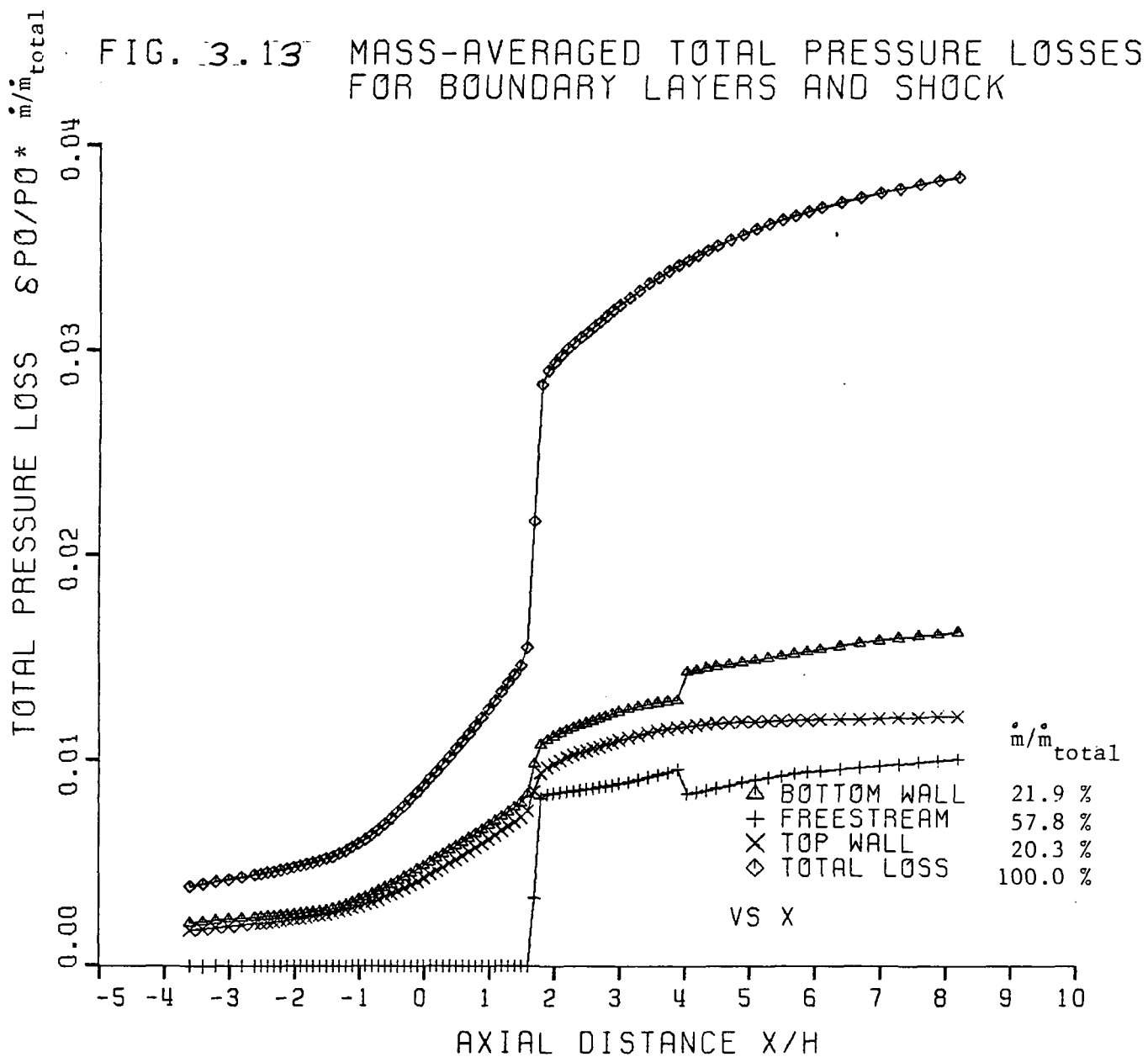


FIG. 3.14 TOTAL PRESSURE LOSS FOR  
SAJBEN DIFFUSER SHOCK VS TOTAL LOSS

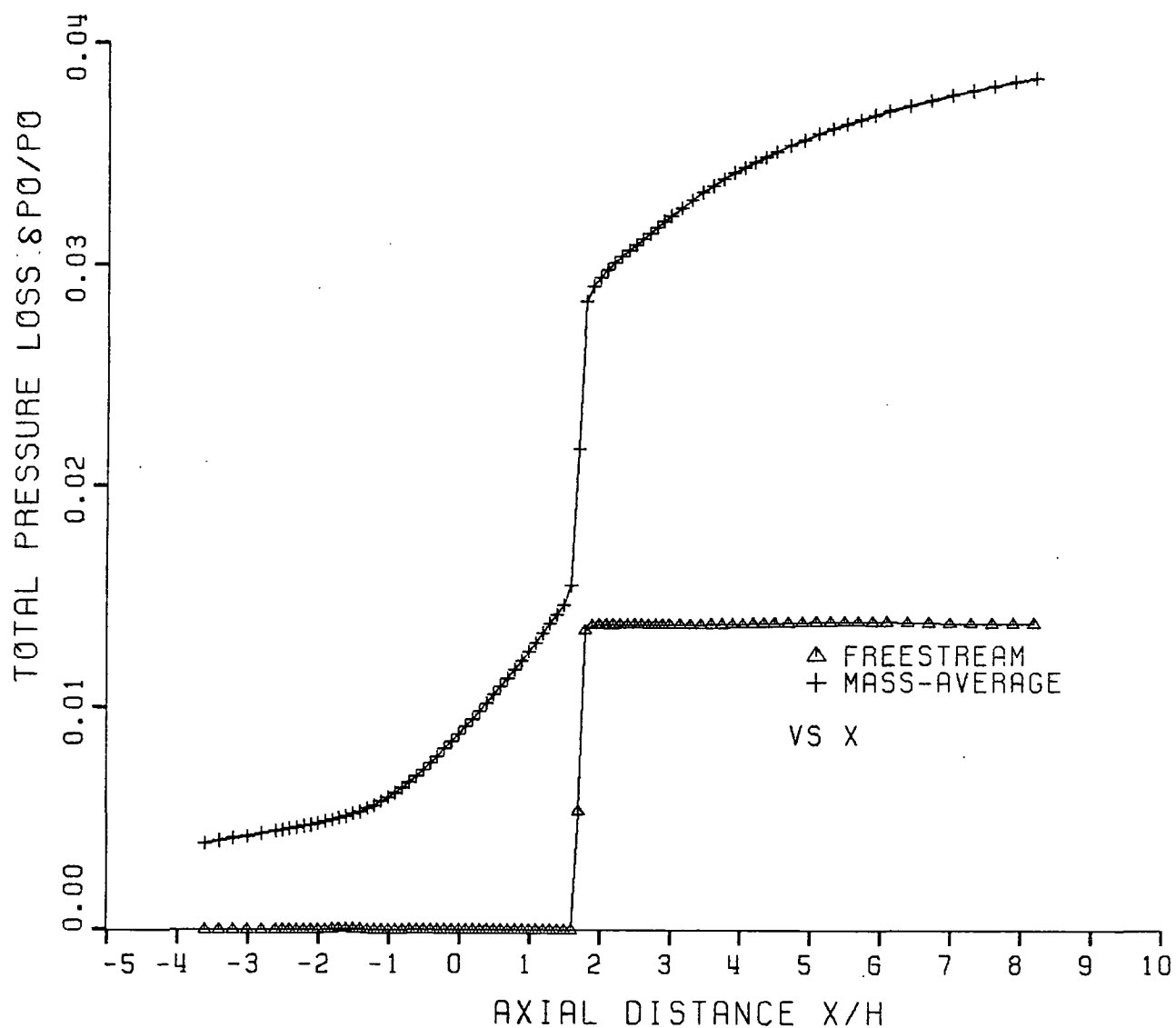
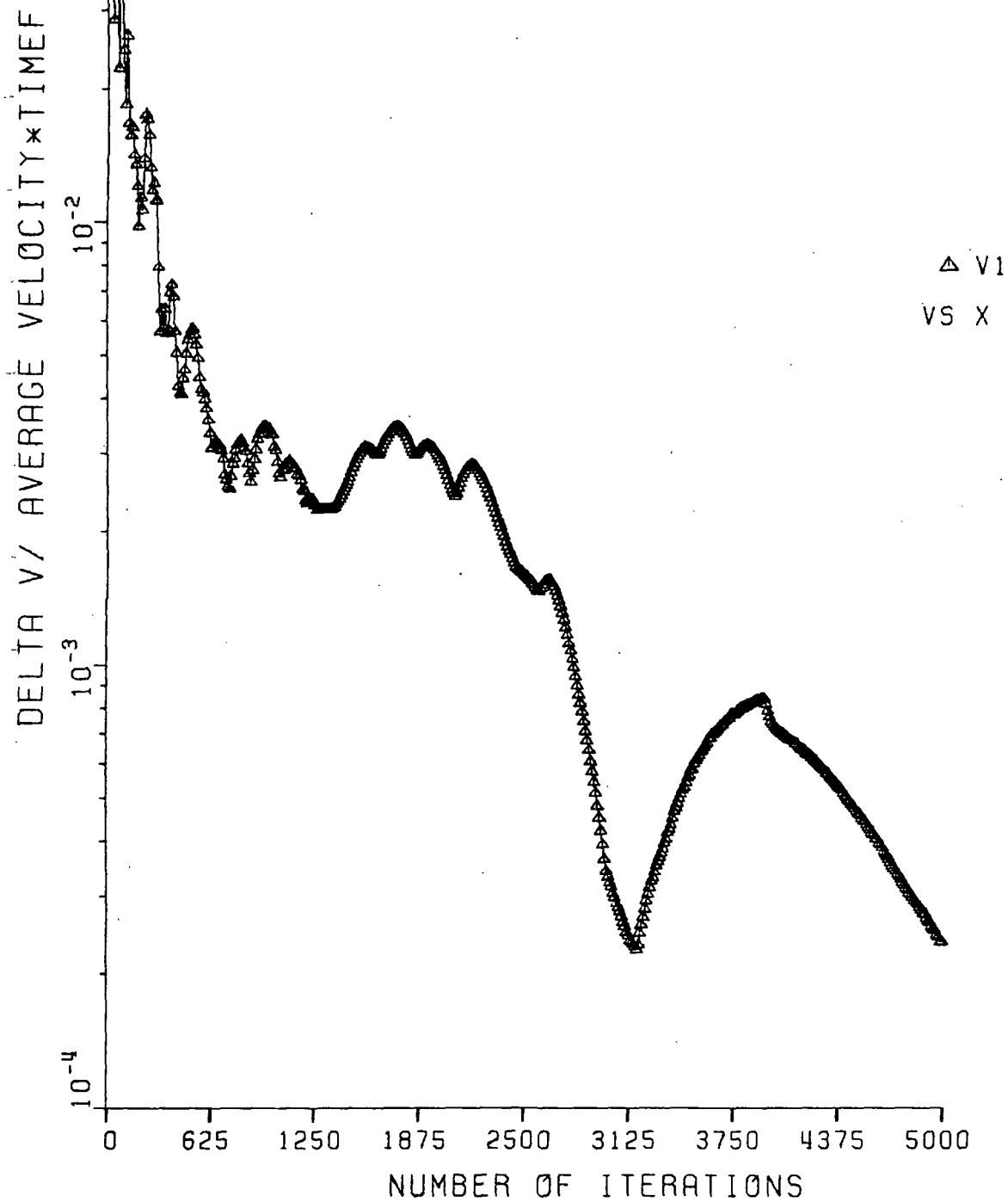
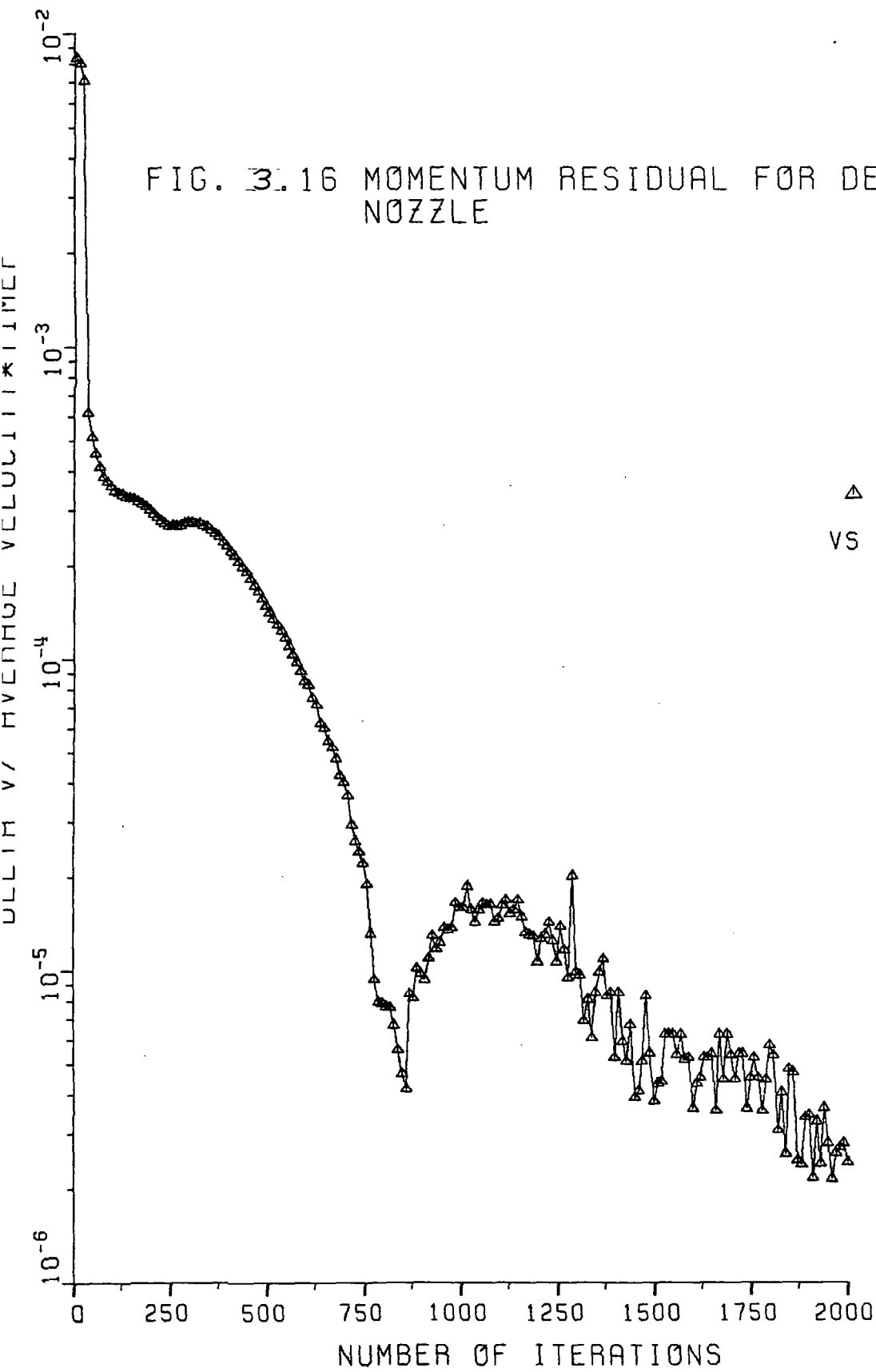


FIG. 3.15 MOMENTUM RESIDUAL FOR SAJBEN  
DIFFUSER







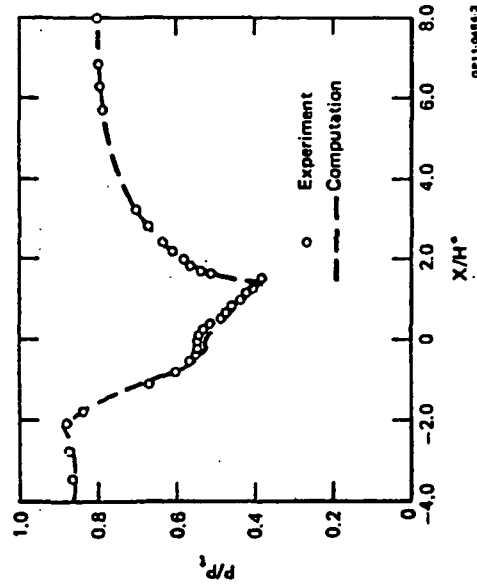


Fig. 6 Surface pressure distribution on upper wall. Model G.  
 $R_p = 0.8$ ,  $\gamma_\infty = 10/9$ ,  $Pr_k = Pr_\omega = 1.0$

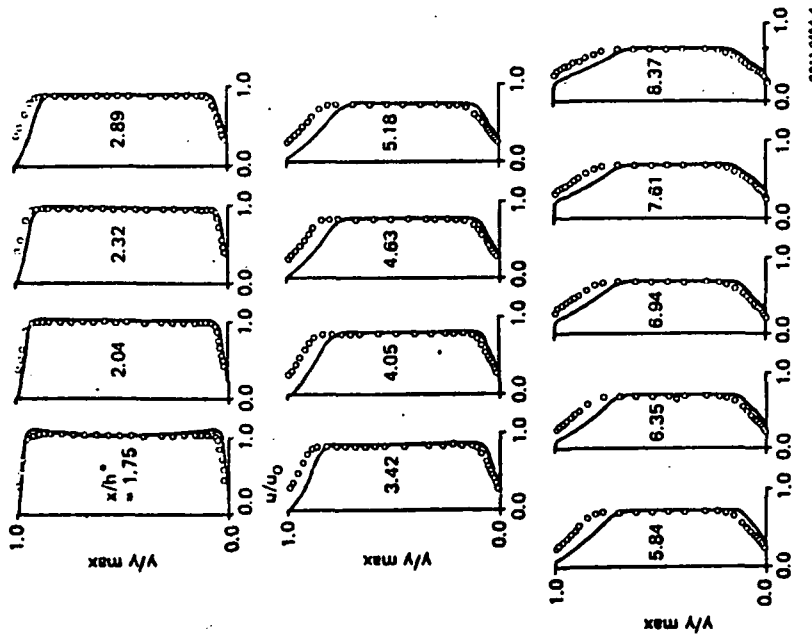


Fig. 7 Computed and measured velocity profiles. Model G.  
 $R_p = 0.80$ ,  $U_0 = 274$  m/s,  $\gamma_\infty = 10/9$ ,  
 $Pr_k = Pr_\omega = 1.0$

Fig. 3.17 Sample Results from Liou, Coakley, and Bergmann (8)

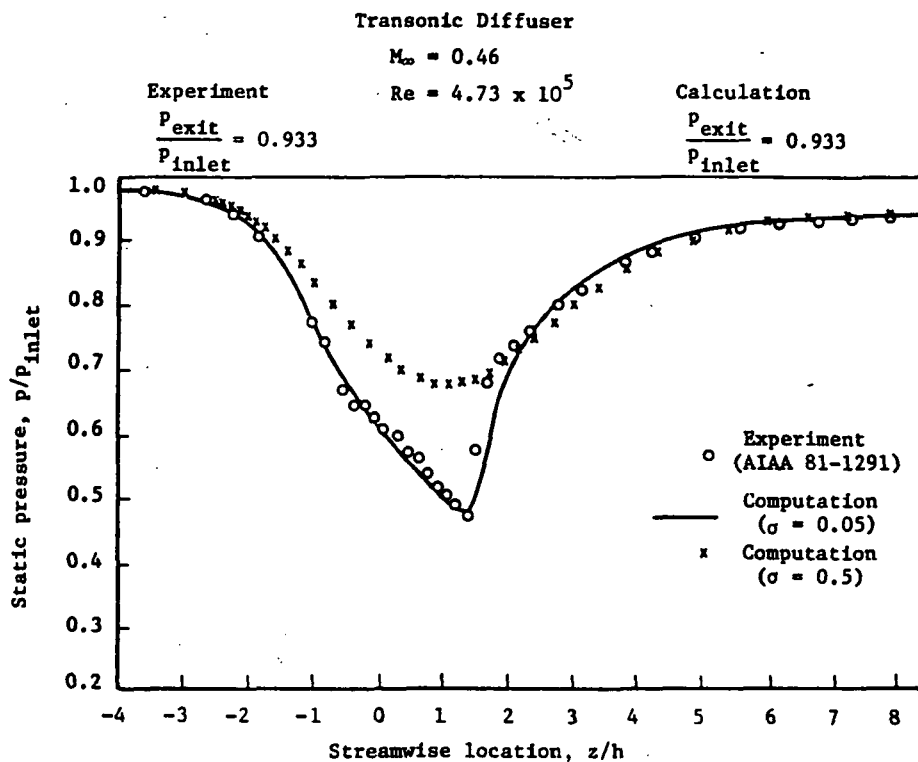
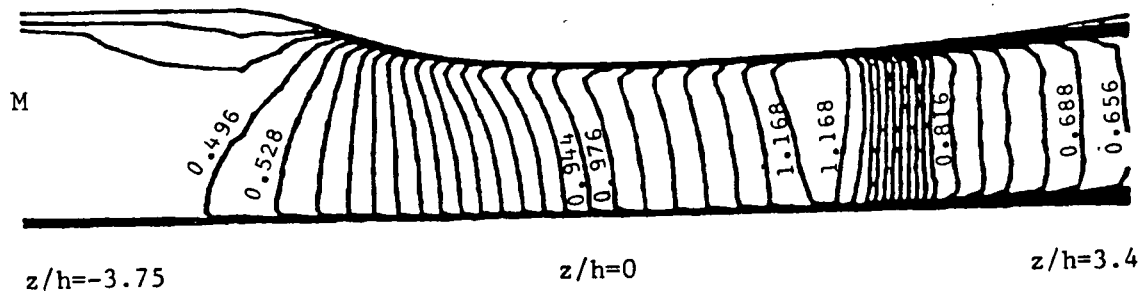
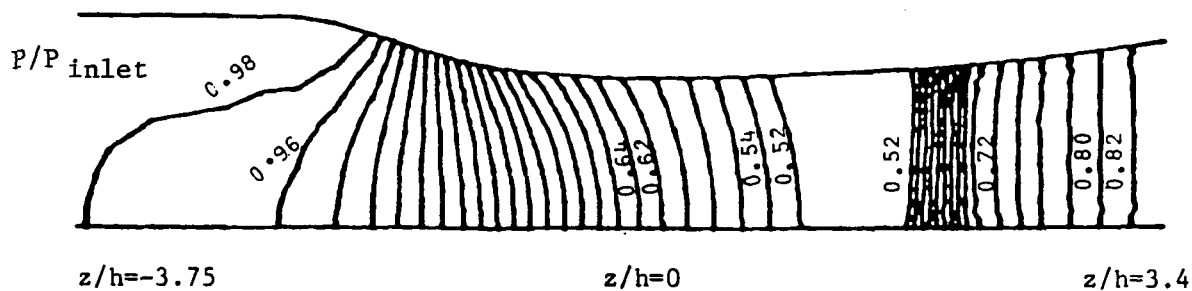


Fig. 5 - Bottom wall static pressure distribution.



(b) Transonic diffuser



(b) Transonic diffuser

Fig. 3.18 Sample Results from Liu, Shamroth, and McDonald (9)

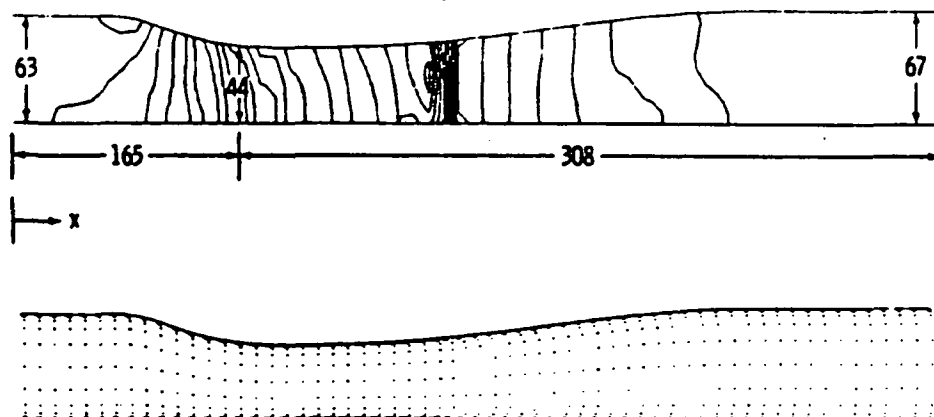


**Fig. 2** Pressure contours and velocity vector field in inlet for turbulent flow ( $P_0/P_i = 0.933$ ,  $M_i \approx 0.46$ ).

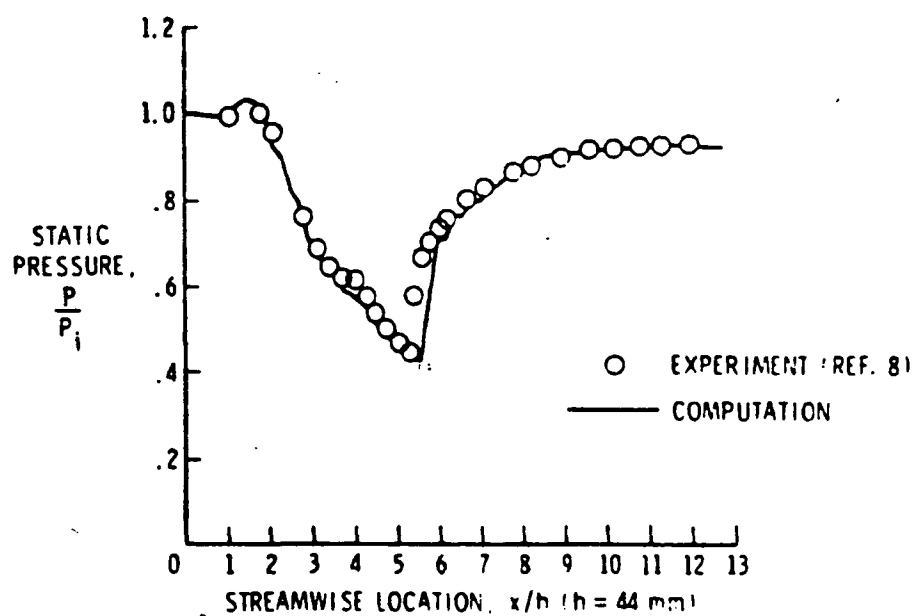


**Fig. 3** Pressure distributions on the top surface of the inlet for turbulent flow ( $M_i \approx 0.46$ ).

Fig. 3.19 Sample Results from Talcott and Kumar (10)

## REFERENCES

1. Nicholson, S., "Development of a Finite Volume Time Marching Method," V.P.I. & S.U. Turbomachinery Research Group Report No. JM/85-3, February 1985.
2. Nicholson, S. and Moore, J. "Extension of a Finite Volume Method to Laminar and Turbulent Flow," V.P.I. & S.U. Turbomachinery Research Group Report No. JM/85-6, June 1985.
3. Moore, J., Nicholson, S., and Moore, J.G. "Development of the Finite-Volume Time Marching Method For Improved Shock Capturing and Reduced Numerical Losses," V.P.I. & S.U. Turbomachinery Research Group Report No. JM/85-11, December 1985.
4. Moore, J.G., Personal Communication
5. Cebeci, T. and Bradshaw, P. Momentum Transfer in Boundary Layers, Hemisphere Publishing Corporation 1977.
6. Bogar, T.J., Sajben, M. and Kroutil, J.C., "Characteristic Frequency and Length Scales in Transonic Diffuser Flow Oscillations," AIAA Paper 81-1291.
7. Salmon, J.T., Bogar, T.J., and Sajben, M. "Laser Velocimeter Measurements in Unsteady, Separated, Transonic Diffuser Flows," AIAA Paper 81-1197.
8. Liou, M.S., Coakley, T.J., and Bergmann, M.Y., "Numerical Simulation of Transonic Flow in Diffusers," AIAA Paper No. 81-1240.
9. Liu, N.-S., Shamroth, S.J., and McDonald, H., "Numerical Solutions of Navier-Stokes Equations for Compressible Turbulent Two/Three Dimensional Flows in the Terminal Shock Region of an Inlet /Diffuser," NASA Contractor Report 3723, August 1983.
10. Talcott, N.A., and Kumar, A., "Two-Dimensional Viscous Simulation of Inlet/Diffuser Flows with Terminal Shocks," Journal of Propulsion, Vol. 1, No. 2, March-April 1985.

## APPENDIX A

To calculate the velocity gradient,  $\nabla u_L$ , for a nonorthogonal grid system, we must be able to transform gradients in the grid directions (I,J, and K) into gradients in the coordinate directions (x,y, and z). From the transformation law of a vector, the gradient of a scalar in one coordinate system can be related to the gradient in another coordinate system using the direction cosines between the two coordinate systems. We will use the cartesian system as our base coordinate system here. Let  $\underline{D}_I, \underline{D}_J$ , and  $\underline{D}_K$  be directional vectors which have a direction parallel with the non-orthogonal coordinate system and span a unit change in I,J, or K respectively. These vectors are shown in Fig. A1. They can be described in terms of their cartesian components. In other words, we can represent them as

$$\underline{D}_I = a_1 \underline{i} + b_1 \underline{j} + c_1 \underline{k} \quad (A.1)$$

$$\underline{D}_J = a_2 \underline{i} + b_2 \underline{j} + c_2 \underline{k} \quad (A.2)$$

$$\underline{D}_K = a_3 \underline{i} + b_3 \underline{j} + c_3 \underline{k} \quad (A.3)$$

where  $\underline{i}, \underline{j}$ , and  $\underline{k}$  are unit vectors in the cartesian coordinate directions, and a,b, and c are the magnitudes of the components of the directional vectors.

The change of a variable ,u, from one point to another within a grid system can be represented as

$$\frac{\partial u}{\partial I} = u_{I+1} - u_I = \int_I^{I+1} d\underline{r} \cdot \nabla u \quad (A.4)$$

where  $\underline{r}$  is a position vector between the two nodes. Rather than dealing with a local derivative in a continuum , we are dealing with approximations of derivatives using finite changes. If the directional vector,  $\underline{D}_I$ , is chosen such that its termini correspond to the nodes at which the properties are evaluated in Eq. A.4, and taking  $\nabla u$  as uniform between grid points,

$$\frac{\partial u}{\partial I} = (r_{I+1} - r_I) \cdot \nabla u. \quad (A.5)$$

But  $\underline{D}_I = r_{I+1} - r_I$  therefore,

$$\frac{\partial u}{\partial I} = \underline{D}_I \cdot \nabla u \quad (A.6)$$

$$\frac{\partial u}{\partial J} = \underline{D}_J \cdot \nabla u \quad (A.7)$$

$$\frac{\partial u}{\partial K} = \underline{D}_K \cdot \nabla u \quad (A.8)$$

where I,J, and K are the coordinate indices for the non-orthogonal coordinate system. Expanding equations A6,A7, and A8, we get

$$\frac{\partial u}{\partial I} = a_1 \frac{\partial u}{\partial x} + b_1 \frac{\partial u}{\partial y} + c_1 \frac{\partial u}{\partial z} \quad (A.9)$$

$$\frac{\partial u}{\partial J} = a_2 \frac{\partial u}{\partial x} + b_2 \frac{\partial u}{\partial y} + c_2 \frac{\partial u}{\partial z} \quad (A.10)$$

$$\frac{\partial u}{\partial K} = a_3 \frac{\partial u}{\partial x} + b_3 \frac{\partial u}{\partial y} + c_3 \frac{\partial u}{\partial z} \quad (A.11)$$

where  $a_1 = D_{Ix}$ , the x component of  $\underline{D}_I$ ;  $b_1 = D_{Iy}$  etc... Equations A9,A10, and A11 can be combined into a single matrix equation,

$$\begin{pmatrix} \frac{\partial u}{\partial I} \\ \frac{\partial u}{\partial J} \\ \frac{\partial u}{\partial K} \end{pmatrix} = \begin{bmatrix} a_1 & b_1 & c_1 \\ a_2 & b_2 & c_2 \\ a_3 & b_3 & c_3 \end{bmatrix} \cdot \begin{pmatrix} \frac{\partial u}{\partial x} \\ \frac{\partial u}{\partial y} \\ \frac{\partial u}{\partial z} \end{pmatrix} \quad (A.12)$$

For the calculation of viscous stresses, Eq. 1.5, we need the gradients of velocity,  $\nabla u_i$ , in cartesian coordinates. To obtain this gradient, we need to take the inverse of the above matrix  $[A]$ , in other words,

$$\begin{pmatrix} \frac{\partial u}{\partial x} \\ \frac{\partial u}{\partial y} \\ \frac{\partial u}{\partial z} \end{pmatrix} = \begin{bmatrix} a_1 & b_1 & c_1 \\ a_2 & b_2 & c_2 \\ a_3 & b_3 & c_3 \end{bmatrix}^{-1} \begin{pmatrix} \frac{\partial u}{\partial I} \\ \frac{\partial u}{\partial J} \\ \frac{\partial u}{\partial K} \end{pmatrix} \quad (A.13)$$

The inverse of matrix A,  $[A]^{-1}$ , will now be determined. From linear algebra,

$$[A]^{-1} = \frac{1}{|A|} (\text{adj}[A]) \quad (A.14)$$

where  $|A|$  is the determinant of  $[A]$  and  $\text{adj}[A]$  is the adjoint of  $[A]$ . The determinant of  $[A]$  is

$$\det[A] = \begin{vmatrix} a_1 & b_1 & c_1 \\ a_2 & b_2 & c_2 \\ a_3 & b_3 & c_3 \end{vmatrix} =$$

$$a_1 \begin{vmatrix} b_2 & c_2 \\ b_3 & c_3 \end{vmatrix} - b_1 \begin{vmatrix} a_2 & c_2 \\ a_3 & c_3 \end{vmatrix} + c_1 \begin{vmatrix} a_2 & b_2 \\ a_3 & b_3 \end{vmatrix} =$$

$$a_1(b_2c_3 - b_3c_2) - b_1(a_2c_3 - a_3c_2) + c_1(a_2b_3 - a_3b_2) \quad (A.15)$$

This can be identified as

$$\det[A] = D_I \cdot (D_J \times D_K) \quad (A.16)$$

Now let us represent the adjoint of A,  $\text{adj}[A]$ , in the form

$$\text{adj}[A] = \begin{bmatrix} A_{11} & A_{12} & A_{13} \\ A_{21} & A_{22} & A_{23} \\ A_{31} & A_{32} & A_{33} \end{bmatrix} \quad (A.17)$$

where the components of the adjoint matrix are

$$A_{11} = \begin{vmatrix} b_2 & c_2 \\ b_3 & c_3 \end{vmatrix} = b_2 c_3 - b_3 c_2 \quad (A.18)$$

However,  $A_{11}$ , can be identified as the x-component of  $\underline{D}_J \times \underline{D}_K$ , in other words,

$$b_2 c_3 - b_3 c_2 = \text{x component of } \underline{D}_J \times \underline{D}_K \quad (A.19)$$

The components of the adjoint matrix,  $A_{12}$  and  $A_{13}$ , are the y and z components of  $\underline{D}_J \times \underline{D}_K$ . Both the results from the numerator and denominator of Eq. A.12, lead to the result that

$$\nabla u_L = \frac{\underline{D}_J \times \underline{D}_K}{\underline{D}_I \cdot (\underline{D}_J \times \underline{D}_K)} \frac{\partial u_L}{\partial I} + \frac{\underline{D}_K \times \underline{D}_I}{\underline{D}_I \cdot (\underline{D}_J \times \underline{D}_K)} \frac{\partial u_L}{\partial J} + \frac{\underline{D}_I \times \underline{D}_J}{\underline{D}_I \cdot (\underline{D}_J \times \underline{D}_K)} \frac{\partial u_L}{\partial K} \quad (A.20)$$

This result can be generalized to the other two components of velocity, v and w. This is the result that is used to calculate velocity gradients in the current program.



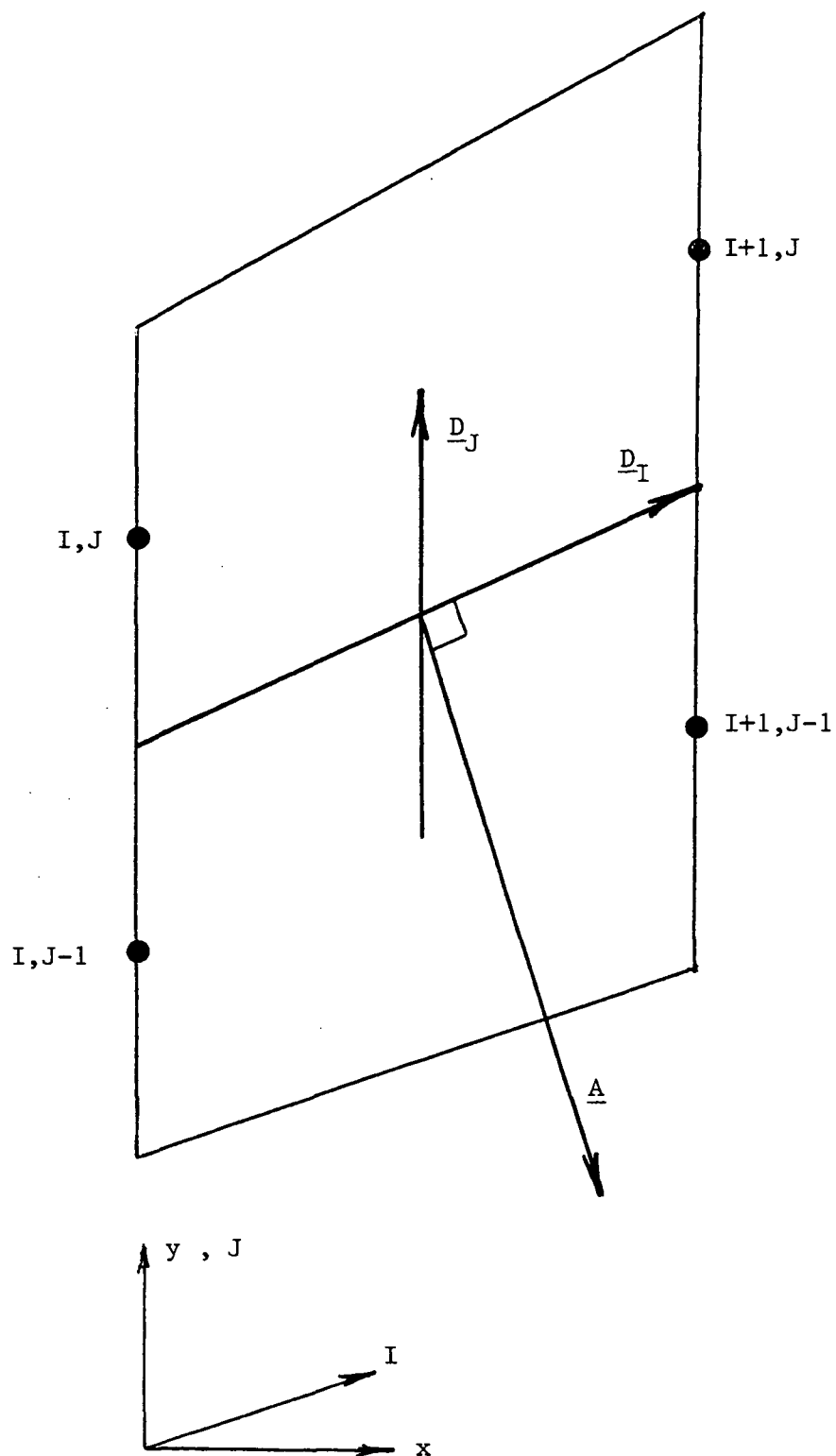


Fig. A1 Identification of Directional Vectors